Impacts of Global Warming on Meiyu-Baiu Extreme Rainfall and the Associated Mid-latitude Synoptic-scale Systems over East Asia Based on 20km-AGCM Simulations

SO, Ka Wai

A Thesis Submitted in Partial Fulfilment

of the Requirements for the Degree of

Master of Philosophy

in

Earth and Atmospheric Sciences

The Chinese University of Hong Kong

September 2019

Thesis Assessment Committee

Professor LEE Shing Yip (Chair)

Professor TAM Chi Yung Francis (Thesis Supervisor)

Professor TAI Pui Kuen Amos (Committee Member)

Professor CHANG Edmund Kar-Man (External Examiner)

Abstract of thesis entitled:

Impacts of Global Warming on Meiyu-Baiu Extreme Rainfall and the Associated Mid-latitude Synoptic-scale Systems over East Asia Based on 20km-AGCM Simulations

Submitted by **SO, Ka Wai**

for the Degree of **Master of Philosophy in Earth and Atmospheric Sciences**

at The Chinese University of Hong Kong in **September 2019**.

Abstract

The aim of this thesis is to study the impacts of global warming on Meiyu-Baiu extreme rainfall and the associated mid-latitude synoptic-scale weather systems over the Eastern China (EC) and the Baiu rainband (Bu) regions in East Asia, based on simulations from the 20-km Meteorological Research Institute atmospheric general circulation model (MRI-AGCM3.2S). This model was demonstrated to give realistic Asian summer monsoon rainfall, as compared with the Tropical Rainfall Measuring Mission (TRMM), and also the Asian Precipitation-Highly-Resolved Observational Data Integration Towards Evaluation (APHRODITE) datasets. Here we used a novel wave-selection algorithm based on the 300hPa wind, in order to identify upper-level propagating wave signals in conjunction with the occurrence of extreme precipitation in either EC or Bu (whenever the grid-scale daily precipitation is above the 95th percentile value). The same algorithm was applied for both the present (1979-2003) and future (2075-2099) climate simulations from the AGCM, so as to infer the impacts of global warming on the behavior of these systems.

Results show that there is robust decrease of intensity of systems influencing both Bu and EC in the future climate. Their corresponding low-to-mid level circulation,

as revealed by low-level convergence, relative vorticity and sea-level pressure composites, is also projected to be weakened. The weakening of these systems is likely due to changes in background circulation in the future over the East Asian mid-latitude zone, such as the widespread increment of the seasonal mean static stability, and the weaker magnitude of the low-level meridional temperature gradient in EC. However, the wave-associated anomalous precipitation over these regions intensifies in the globally warmed future. This is mainly due to enhanced contribution from extreme rainfall, which increases as the background temperature in these regions warms, largely following the Clausius-Clapeyron relation. Therefore, changes of wave-related extreme precipitation in EC and Bu are mainly due to the thermodynamic effect; the latter appears to be much stronger than the potential impacts due to the slight weakening of these weather systems.

摘要

本研究旨在透過分析日本氣象廳氣象研究所的二十公里解析度大氣模型（MRI-AGCM ）的數據，探討全球暖化對華東地區及日本梅雨區在梅雨期間之極端降水及其相關的中緯度天氣尺度系統的影響。透過與 TRMM 及 APHRODITE 數據的比較，該模型被證實能夠模擬出真實的亞洲夏季季風降雨。在此，我們使用一個基於 300 百帕斯卡風場的新波動選取演算法，識別與華東地區或日本梅雨區出現的極端降水（當任一網格點的日降水超過其 95 百分數數值）相關的高層傳播波訊號。相同的演算法會運用於該模型對現時及未來的氣候模擬當中，以推斷全球暖化對這些系統狀態的影響。

結果顯示，在未來氣候中影響華東地區及日本梅雨區的系統將會顯著減弱。它們對應的低至中層環流，例如低層幅合、相對渦度及海平面氣壓的合成圖，亦同樣預測會出現減弱。這些系統的減弱很可能由於東亞中緯度地區的背景環流在未來的改變，例如廣泛地區季節平均靜態穩定度增強，以及較弱的華東地區低層緯向温度梯度。不過，這些地區與波動相關的異常降水在未來全球變暖下將會出現增強。這主要由於來自極端降水的比例隨著這些地區的背景温度變暖而增加，並大致與 Clausius-Clapeyron relation 吻合。因此，在華東地區及日本梅雨區與波動相關的極端降水之改變主要來自熱力性影響，後者似乎比由於這些天氣系統減弱所導致的潛在影響強烈得多。

Acknowledgement

Foremost, I would like to express my sincere gratitude to my thesis supervisor Professor Francis Tam for his incessant support and precious guidance. He's very patient in receiving updates of research progresses, without imposing any limitation on my freedom. His abundant experience and immense knowledge in atmospheric studies always steered me in the right direction whenever I needed it. I wouldn't have finished this project so quickly without his multitudinous assistance. I would like to thank Professor Gabriel Lau, who shared with us the MRI-AGCM dataset, greatly deepened my understandings on different systems and circulations within the atmosphere, and helped reviewing my thesis. I would also like to thank Professor Amos Tai and Professor Joe Lee, both of which took their pleasant time to comment on my work during review.

I would like to thank the Department of Earth System Science Programme. My research work can only be done successfully with the aid of its friendly staff, as well as under such a comfortable learning environment. Last but not least, I would like to thank all my groupmates during this 2-year study. Our continuous academic discussions brought a lot of pleasure to this research, and our mutual encouragement made the work particularly unforgettable.

Table of Contents

List of Figures

1. Introduction

1.1 Meiyu-Baiu

East Asian summer monsoon is a subtropical monsoon in which the low-level winds reverse mainly from wintertime northerlies to summertime southerlies (e.g. Wang and Lin, 2002). Starting with the rainfall surges over the South China Sea in mid-May, the northward advancement of the monsoon rain belt undergoes three standing stages, which are separated by two stages of abrupt northward jump (Ding and Chan, 2005). The second stationary stage is characterized by the initiation of the Meiyu-Baiu rainy season in early to mid-June. In fact, Meiyu-Baiu is the major rainy season which accounts for the period of peak precipitation over Yangtze River-Huaihe River basin (e.g. Ding et al., 2007) and southwestern Japan (e.g. Ninomiya and Akiyama, 1992). Meiyu in China and Baiu in Japan are brought by an elongated rainband from June to mid-July, which is usually quasizonally oriented near 30N over eastern China and tilts east-northeastward toward Korea and Japan (Ding and Sikka, 2006). Such rainband is usually characterized by a low-pressure trough, which represents a weak stationary surface front with significant horizontal wind shear across the front and frequent occurrence of prolonged heavy rainfall. On the other hand, the rainband is accompanied by sharp moisture gradients near the surface due to abundant moisture transport from southwesterly airstream, and a westerly jet tilted northward with height (e.g. Ninomiya and Shibagaki, 2007; Sampe and Xie, 2010).

Sampe and Xie (2010) found that various environmental forcings determine the formation of the Meiyu-Baiu rainband. According to their findings, such rainband is anchored by the westerly jet in two ways. One is that the horizontal warm advection by the westerlies from the eastern flank of the Tibetan Plateau lead to adiabatic induction of ascending motion, which induces convection and is in turn strengthened

by the corresponding condensational heating. It explains the termination of the Meiyu-Baiu in late July because abrupt northward movement of westerly jet greatly weakens such warm advection. Another way is that the steering transient disturbances in the westerlies provides phases favorable for convection through convective instability and adiabatic updrafts. This explains the occurrence of active convection in the region of relatively weak mean instability. Besides, the Pacific subtropical high pressure and the Asian heat low bring lots of moisture to eastern China by the low-level southerlies in between, which also serve as one of the external environmental forcings for the Meiyu-Baiu rainband. Although the convection over southern China is fed by the moisture transport as early as April (Ding and Chan, 2005), sea surface warming in the northwestern Pacific determines June to mid-July as the main period for Meiyu-Baiu. The Tibetan Plateau is also conducive to the formation of Meiyu-Baiu by anchoring warm advection along the westerly, intensifying southerlies over China, and generating eddies on its eastern flank.

Although Meiyu over China and Baiu over Japan occur almost concurrently in the early summer, their frontal structure and dynamics exhibit lots of differences (e.g. Chen and Chang, 1980; Ding, 1992; Ding et al., 2007; Ninomiya and Shibagaki, 2007; Sampe and Xie, 2010). Chen and Chang (1980) indicated that the cross sections of southern East China Sea and southern Japan resemble a typical midlatitude baroclinic front with strong vertical tilting, upper level cold core and strong horizontal temperature gradient, while the section of southeastern China resembles a semitropical disturbance with equivalent barotropic warm core structure, weak horizontal temperature gradient, and rather strong horizontal wind shear in the lower troposphere. Ding (1992) summarized that the Meiyu front is related to a shear line between the southerly and northerly winds in the low levels. Furthermore, intense Meiyu rainfall is

induced by successive passage and development of a medium-scale frontal depression, whereas the Baiu front is generated by several clearly separated medium-scale depressions, some of which may further develop into significant frontal cyclones if the thermal gradient is strong. Different geographical locations of Meiyu and Baiu help explains the more significant influence of summer monsoon in the former (Ding et al., 2007), and the existence of sub-synoptic scale depression in the latter due to short waves (Ninomiya and Shibagaki, 2007).

1.2 Mid-latitude synoptic-scale systems

Migratory synoptic-scale waves are one of the important weather systems influencing surface weather in the mid-latitudes (e.g. Davies, 2015). These waves are fast-moving baroclinic wave disturbances, characterized by propagation of synoptic-scale meridional undulations in velocity and pressure field under background westerlies flow in the upper-level. They interact with surface baroclinity, in the way that the axes of trough and ridge tilt westward with height, while the axes of warmest and coldest air tilt in the opposite direction. Such interaction creates associated low-level cyclones (e.g. extratropical cyclones) and anticyclones, forming storm track regions in the mid-latitudes (e.g. Hoskins et al., 1985). Mid-latitude synoptic-scale waves propagate eastward in the timescale of few days to about one week while long waves are slowly moving, stationary or even retrograde. The former can be identified as the transient short waves embedded in and moving along the prevailing westerly flow within the latter.

Baroclinic disturbances grow due to baroclinic instability, which is mainly determined by the vertical shear of zonal wind and the static stability (Eady, 1949; Hoskins and Valdes, 1990). Such vertical wind shear, and westerly flow that is

unstable to small perturbations, are indeed generated by the strong meridional temperature gradient in the mid-latitudes. The growth mechanism due to such wave instability comes from conversion of available potential energy to kinetic energy, which can be conceptualized by potential vorticity thinking (Hoskins et al., 1985). The transient eddies (cyclones and anticyclones) in the mid-latitudes are therefore responsible for massive meridional transports of heat, moisture and momentum. Based on both observations and model simulations, Coumou et al., (2015) calculated high-pass filtered total kinetic eddy energy (EKE) and found consistency between the trend of summertime EKE and pole-to-mid-latitude thermal gradient. Due to the seasonality of such gradient, summertime extratropical storms in the Northern Hemisphere have longer lifetime and tend to be weaker than their winter counterparts (e.g. Mesquita et al., 2008). Nonetheless, static stability also plays an important role in modulating the amplitude of baroclinic response. The low static stability helps to explain the spring prosperity of baroclinity over Southern Hemisphere (Walland and Simmonds, 1999), and also the synoptic-scale transient eddy activity over East Asia (Ren et al., 2010).

Eddies associated with upper-level travelling wave is related to weather extremes in the mid-latitudes (e.g. Romero, 2006; Coumou et al., 2015; Lehmann and Coumou, 2015; Raveh-Rubin and Wernli, 2015; R. Barbero et al., 2018). The wind related to extratropical cyclones can be very intense (Raveh-Rubin and Wernli, 2015), which can lead to extensive destruction say over Europe (Fink et al., 2009). Hewson and Neu (2015) conceptualized the strongest winds in extratropical cyclone into three belt jets whose gust strength ranges from 50 to 90 knots. Such strong wind is related to the interaction between cyclonic circulation and large-scale winds and redistribution of eddy kinetic energy (Rivière et al., 2015). The other major impact associated with the upper-level travelling wave is extreme precipitation. Lehmann and Coumou (2015)

found that monthly precipitation extremes are associated with significantly higher EKE in all mid-latitude continental regions, and such linkage is robust based on different observation data. Extratropical extreme rainfall is highly relevant to the so-called warm conveyor belt (Pfahl et al., 2014; Catto et al., 2015), which is a warm moist airstream traveling poleward parallel to the cold front inside extratropical cyclone, due to intense latent heat release and precipitation formation. In contrast, due to the modulating effect on continental temperature by cyclonic activity and the probable effect on prolonging blocking systems, summer heat extremes (and winter cold extremes) on monthly timescales are associated with low storm track activity over most parts of mid-latitude continental regions (Coumou et al., 2015; Lehmann and Coumou, 2015). Although low monthly EKE implies low variability of weather, it in fact increases the chance of persistent weather conditions and thus is relevant to heat extremes on longer timescales.

1.3 Change of extreme rainfall and mid-latitude synoptic-scale systems under global warming

Observed extreme precipitation over most parts of the globe was found to intensify in the past few decades (e.g. Alexander et al. 2006; Donat et al., 2013; Westra et al., 2013; Donat et al., 2016). The general intensification pattern is projected to continue in the future-warmed climate based on various model simulations (e.g. Sillmann et al., 2013; Donat et al., 2016). Under global warming, the projected change of extreme precipitation is larger than the change of total precipitation (e.g. Allen and Ingram, 2002; Sillmann et al., 2013). According to the Clausius-Clapeyron (CC) relation (e.g. Pall et al., 2007), the saturated vapor pressure increases by 7% per degree K increase of low-tropospheric temperature. It is believed that extreme rainfall also

scales according to the CC-relation, whereas the global mean precipitation is less rapid and constrained by global energy budget (Allen and Ingram, 2002). Emori and Brown (2005) separated projected changes of rainfall into dynamic and thermodynamic components and found that thermodynamic change is more important in determining the rainfall change. However, note that, super-CC scaling for change of rainfall extreme is also reported over Europe (Lenderink and van Meijgaard, 2008), which indicates the possible influences due to other mechanisms such as dynamical effect of weather systems.

Although a number of weather systems can contribute to extreme rainfall (e.g. Utsumi et al., 2017), systems other than tropical cyclones (TCs) are found to dominate the projected increase of extreme precipitation over East Asia (e.g. Utsumi et al., 2016; Lui et al., 2018). In fact, quite a lot of studies focused on the variation of extratropical cyclones, which contribute to most of the extreme precipitation in the mid-latitudes (Hawcroft et al., 2012), based on analysis of observation and model projections (e.g. Wang et al., 2006; Ulbrich et al., 2009; Mizuta et al., 2011). However, only minority of them investigated how summertime extratropical cyclones change due to warming background (Geng and Sugi, 2002), and almost none of them further investigate the projected change of their associated extreme rainfall. Since low-level eddies can be generated by baroclinic interaction with the upper-level waviness, Coumou et al. (2015) studied synoptic-scale wave activity and its projected change under global warming. They found that summertime EKE of synoptic-scale waves decreases mainly due to weakening of vertical wind shear and zonal-mean flow. Although the linkage between upper-level waves and extreme rainfalls has been studied by some researches (e.g. Francis and Vavrus, 2012; Röthlisberger et al., 2016), in-depth analyses on the synoptic-scale systems associated with extreme rainfalls are still limited.

This study is motivated by the above reasons, and also a recent finding from Lui et al. (2018), who found that projected change of summertime extreme rainfall over the Baiu rainband region only follows sub-CC scaling, based on simulations from the 20-km Meteorological Research Institute atmospheric general circulation model (MRI-AGCM3.2S). Our emphasis will be put in investigating how Meiyu-Baiu extreme rainfall over Eastern China (EC) and Baiu rainband (Bu) regions, and their associated mid-latitude synoptic-scale systems change in the projected-warmed future, based on the same AGCM simulations. We will examine how much the dynamical change of mid-latitude synoptic systems is related to the change of rainfall extremes over east Asia, and therefore revealing the relative importance between thermodynamic and dynamical arguments in explaining the change of rainfall extremes. EC and Bu regions are chosen for the analysis because they are strongly influenced by transient eddies within the westerlies during the characteristic Meiyu-Baiu rainy season (e.g. Ninomiya and Shibagaki, 2007; Sampe and Xie, 2010). Moreover, since the geographical location and frontal structure of Meiyu and Baiu are quite different, studying both of the regions allows us to further examine whether the extreme rainfall and the associated systems response differently under various environments during global warming.

2. Model and Data

2.1. AGCM experiments

The MRI-AGCM3.2S is an improved version of the model developed collaboratively by Japan Meteorological Agency (JMA) and Meteorological Research Institute (MRI) (Mizuta et al., 2006; Kitoh et al., 2009). It is a global model with a horizontal grid size of about 20 km and vertical levels of unevenly spacing up to 0.01 hPa, based on the dynamical framework using a hydrostatic primitive equation system. Various parameterization schemes, such as Yoshimura cumulus scheme (Yukimoto et al., 2011), Tiedtke cloud scheme (Tiedtke, 1993) and the radiation scheme used in JMA operational model (JMA, 2007), are introduced for improvement of climate simulation. A comprehensive description and evaluation of the model were given by Mizuta et al. (2012). The present-day (1979-2003) simulation was first made by using monthly-mean sea surface temperature (SST) and sea-ice concentration (SIC) observations from the Met Office Hadley Centre (Rayner et al., 2003) as the lower boundary conditions. The future climate (2075-2099) simulation was then performed by using SST and SIC generated by eighteen models from the Coupled Model Intercomparison Project phase 3 (CMIP3) (Solomon et al., 2007), under the Special Report on Emissions Scenarios (SRES) A1B scenario, as the prescribed lower boundary conditions (Murakami et al., 2012).

2.2. Observation and Reanalysis data

Various precipitation observations and reanalysis data were used for model evaluation in this study. Two observational precipitation datasets, namely the Tropical Rainfall Measuring Mission 3B42 version 7 (TRMM3B42v7) (Huffman et al., 2007) and the Asian Precipitation-Highly-Resolved Observational Data Integration Towards

Evaluation version 1101 (APHRODITEv1101) (Yatagai et al., 2012) were chosen to compare with the simulated rainfall. The TRMM3B42 dataset was produced by combination of satellite-based precipitation estimates and rain gauge-based adjustment (Huffman et al., 2007). The product covers the latitudinal band between 50N and 50S since 1998, at relatively fine scales (0.25° × 0.25°, 3 hourly). The APHRODITE dataset was obtained by interpolation of rain gauge-based precipitation (Yatagai et al., 2012). It provides daily accumulated precipitation from 1951 to 2007, covering monsoon Asia at both 0.25° and 0.5° resolution. Zhao and Yatagai (2014) found that previous version of TRMM3B42 dataset, and the APHRODITE dataset, are generally consistent in representing the spatial and temporal distributions over China. Although they also indicated that the former underestimates light and moderate precipitation in the western China and overestimates heavy precipitation in the southeastern China, its capability of describing precipitation characteristics in fact has been obviously improved in its version 7 (Chen et al., 2013). Throughout the study, daily precipitation values at 0.25° resolution from both the TRMM3B42v7 and APHRODITEv1101 datasets would be used, based on the consideration of synoptic-scale nature of systems that we are going to analyze.

In addition, best track data from the Joint Typhoon Warning Center (JTWC) would be used for examination of historical tropical cyclones (TCs). The data contains 6-hourly basic information of TCs, which have been classified into different intensities based on 1-minute sustained wind speed. Only those reaching at least tropical storm intensity, which corresponds to maximum sustained wind speed not less than 18 ms^{-1}, would be considered in this study. Meanwhile, the ERA-Interim global atmospheric reanalysis data from the European Centre for Medium-Range Weather Forecasts (ECMWF) were used to represent meteorological variables other than precipitation in

different levels. Such reanalysis products, which contain 6-hourly data at 0.75° resolution, were demonstrated to have substantial improvements upon earlier reanalysis product (ERA-40) from ECMWF (Dee et al., 2011). Unless otherwise specified, daily mean values of ERA-Interim reanalysis data would be used in the following parts of study.

3. Model Evaluation

3.1. Total Precipitation

In order to examine the capability of the AGCM in reproducing realistic summer monsoon and precipitation over East Asian monsoon region, precipitation characteristics from present climate simulation are first evaluated. Fig. 3.1 shows the climatological monthly mean precipitation rate from May to September, based on TRMM and present climate simulation respectively. It can be seen that the simulated evolution of Asian summer monsoon, including its northward advance from May to July, and its southward retreat and weakening starting from August, agrees well with the spatiotemporal patterns from observations. In May, major rainfall occurs over eastern part of Bay of Bengal, central-eastern part of Indochina Peninsula and southeastern part of China (Fig. 3.1a). Despite a slight overestimation of rainfall over central China, those features indicating the commencement of East Asian summer monsoon can be well captured by the AGCM (Fig. 3.1b). In June, monsoon rainfall shows an abrupt increase over eastern part of Arabian Sea, Bay of Bengal, South China Sea, southern China and near southern Japan (Fig. 3.1c). It marks the northward advance of summer monsoon, and also the formation of Meiyu-Baiu rainband. All of the above characteristics are reasonably reproduced by the AGCM (Fig. 3.1d). In July, the much weaker Meiyu-Baiu rainband further moves to the northeast China, Korean Peninsula and Japan, while the general monsoon precipitation south of 20N are basically unchanged (Fig. 3.1e). AGCM results are generally consistent with those patterns (Fig. 3.1f). From August to September, the monsoon rainfall over south and east Asia weakens and moves southward slowly (Figs. 3.1g and 3.1i). Accordingly, the precipitation over China continues to weaken but the Japan experiences a second peak of rainfall due to re-intensification of frontal activity. Similar to the earlier

months, the model performance in capturing the last stage of the summer monsoon is generally satisfactory (Figs. 3.1h and 3.1j).

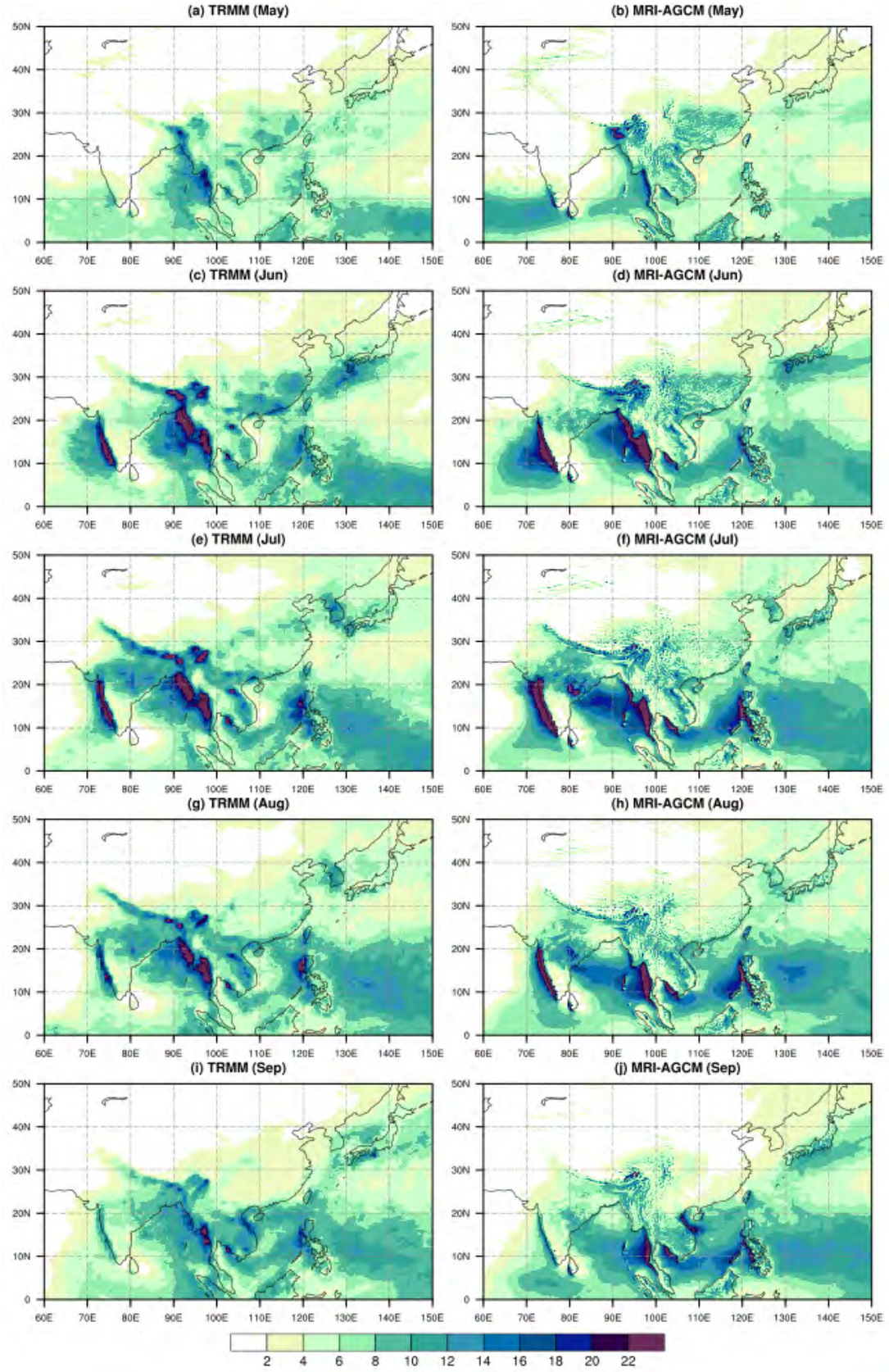

Fig. 3.1: Climatological monthly mean precipitation rate (units: mm day^{-1}) for (a, b) May, (c, d) June, (e, f) July, (g, h) August and (i, j) September, based on (a, c, e, g, i) for TRMM3B42v7 and (b, d, f, h, j) for MRI-AGCM3.2S data for the periods of 1998-2013 and 1979-2003, respectively.

Under the strong influence by the Meiyu-Baiu rainband, temporal variation of precipitation over both EC (25-32N, 108-120E) and Bu (30-35N, 127-143E) regions is another model-simulated characteristic that requires evaluation. Fig. 3.2 shows the area-averaged values of climatological daily mean precipitation rate over EC and Bu, based on observations and simulations, respectively. It can be seen that the temporal revolution of model-simulated mean precipitation over EC closely resembles those based on the two observational datasets (Fig. 3.2a). Both simulations and observations indicate a rainfall peak around June, as well as the light precipitation from October to January. However, the model-simulated precipitation tends to overestimate the rainfall in spring and thus cannot describe a sharp peak of rainfall over EC in June, which is seen in observations. The similarity of temporal variation between model-simulated and observational precipitation is much higher for Bu (Fig 3.2b). Although there still exists small bias between model results and observations in late spring, late summer and autumn, both the primary (around June) and secondary peak (around September) of rainfall over the Baiu region are well captured by the AGCM. In general, the model shows its ability in simulating realistic temporal evolution of precipitation, which includes the start of Meiyu-Baiu season in June over both regions.

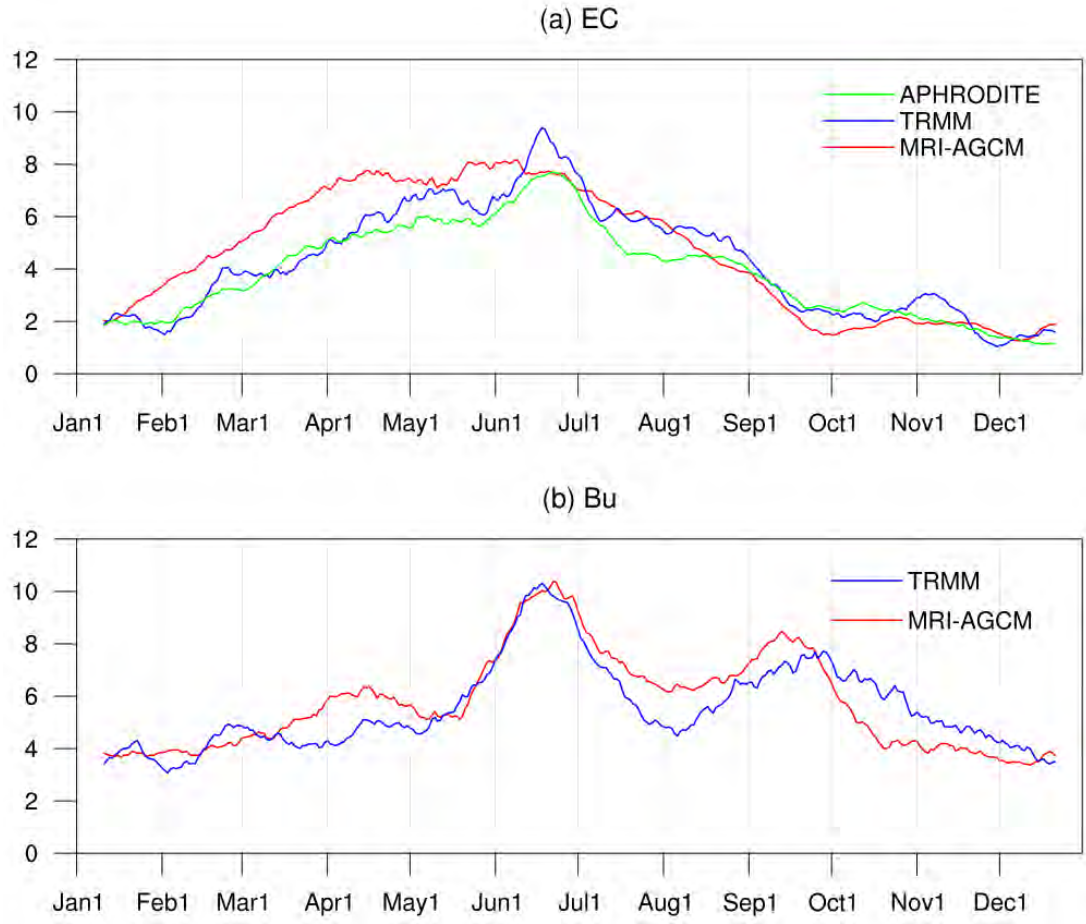

Fig. 3.2: 21-day running mean of climatological daily mean precipitation rate (units: mm day^{-1}), averaged over (a) Eastern China (25-32N, 108-120E) and (b) Baiu rainband (30-35N, 127-143E), based on APHRODITEv1101 and MRI-AGCM3.2S data for the period of 1979-2003, and TRMM3B42v7 for the period of 1998-2013. The values are computed over land area only for APHRODITEv1101.

3.2. Extreme Precipitation

It is also essential to compare model-simulated precipitation extremes with observations. An extreme precipitation event (extreme case) is identified whenever the daily precipitation exceeds the 95th percentile (R95p) of rain rate over wet days. In this study, wet days are defined as days when daily precipitation is greater than 0.1 mm. Figs. 3.3, 3.4 and 3.5 show the climatological decad-mean probability of occurrence of extreme cases from 7th to 24th decad, based on APHRODITE, TRMM and model simulations, respectively. The decad-mean probability is computed by dividing the

total count of extreme cases by the total number of days during that decad. The first six decads and those after the 24th decad are not shown, since their extreme cases are generally irrelevant to the major Meiyu-Baiu rainy season, which approximately lasts from 16th decad (31 May – 9 Jun) to 19th decad (30 Jun – 9 Jul). It can be seen that the occurrence of extreme cases is getting more frequent from 7th to 16th decad over southeastern China and Japan due to frontal activities (Figs. 3.3 and 3.4). An abrupt increase of frequency of extremes over northern part of South China Sea is observed in the 14th decad (Fig. 3.4), followed by an active belt sweeping over China and Japan from south to north in the subsequent couples of decads (Figs. 3.3 and 3.4). The active belt in the simulations also exhibits similar northward movement, but such belt is less clearly defined (Fig. 3.5). Afterwards, both TRMM and model simulations show rareness of extreme cases over southeastern China and south of the Japan since 20th decad. All of those findings demonstrate the overall ability of the AGCM to reproduce reasonable seasonal variation of extreme rainfall.

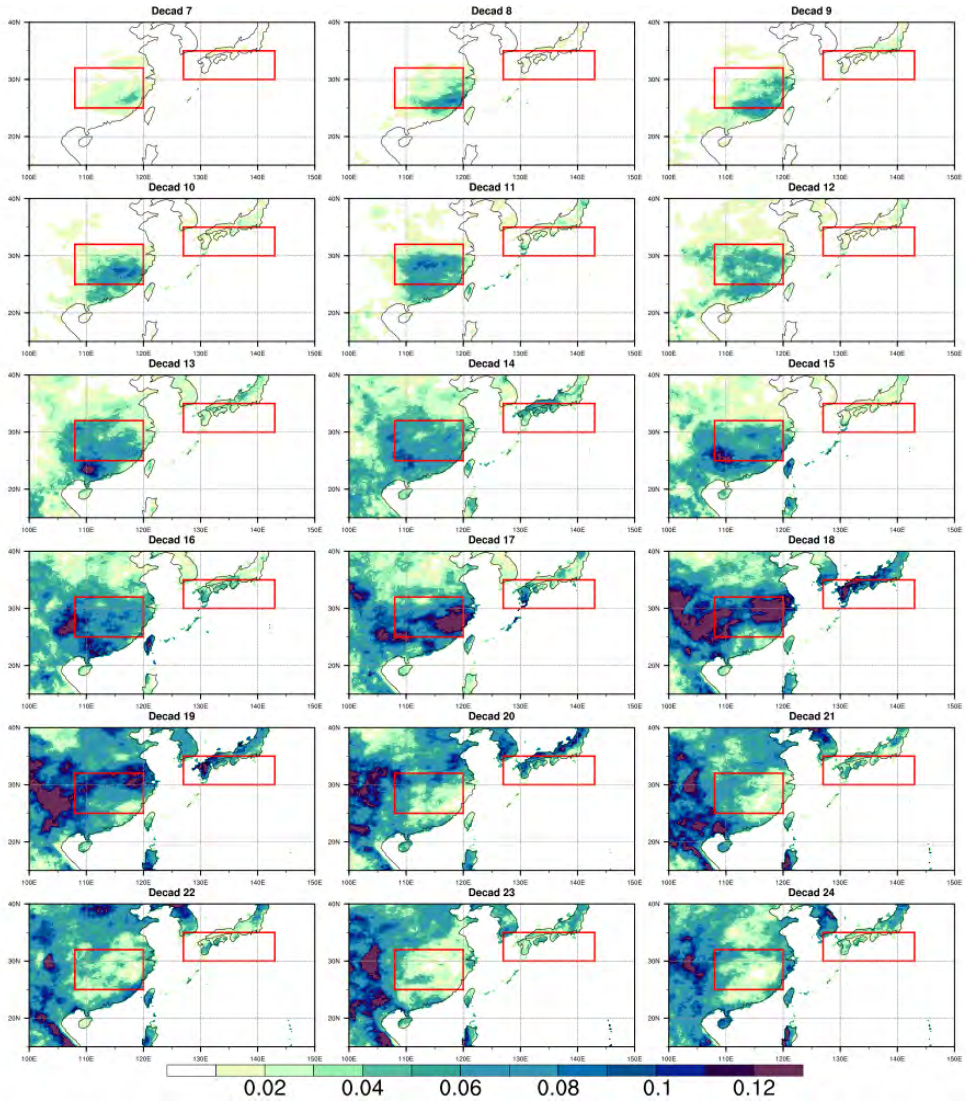

Fig. 3.3: Climatological decad-mean probability of occurrence of extreme cases from 7th to 24th decads based on APHRODITEv1101 for the 1979-2003 period. The values are computed over land area only for APHRODITEv1101.

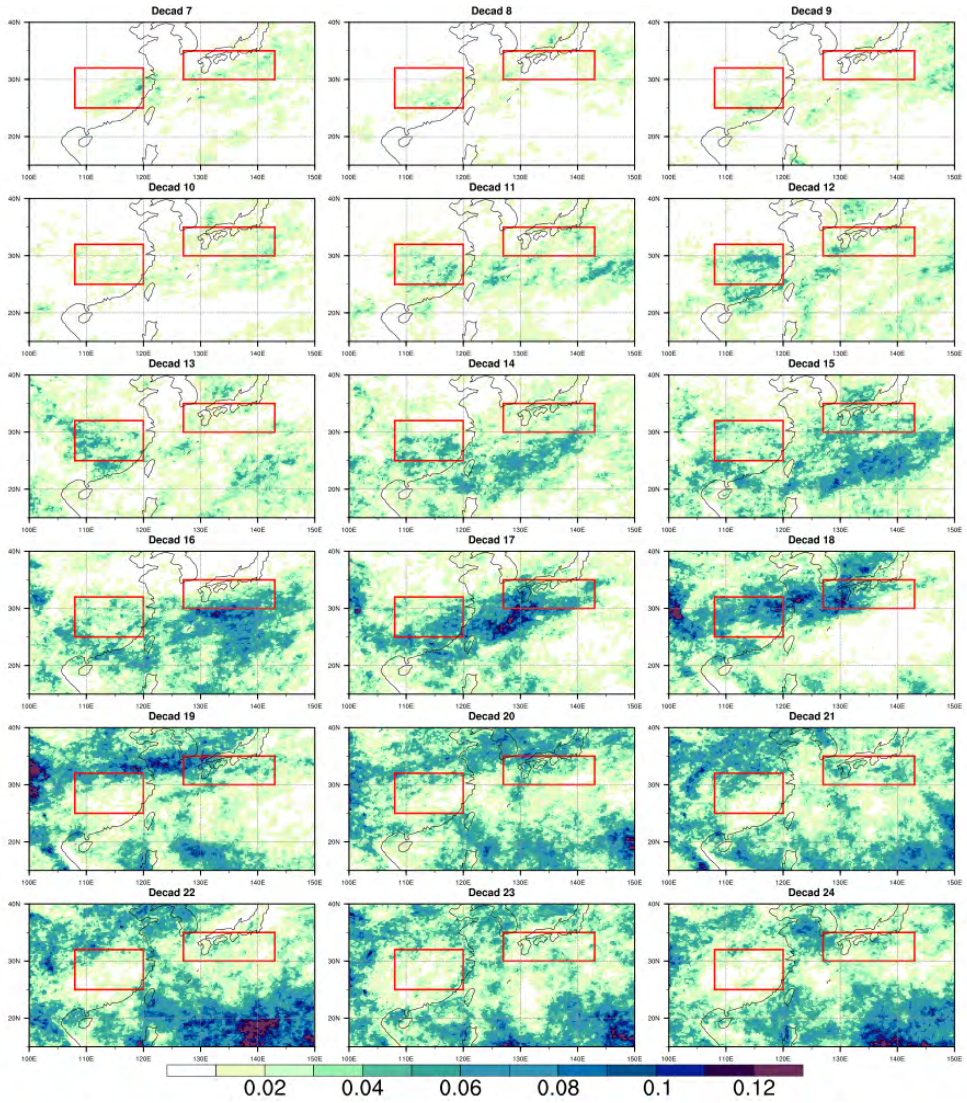

Fig. 3.4: As in Fig. 3.3, but based on TRMM3B42v7 for the 1998-2013 period.

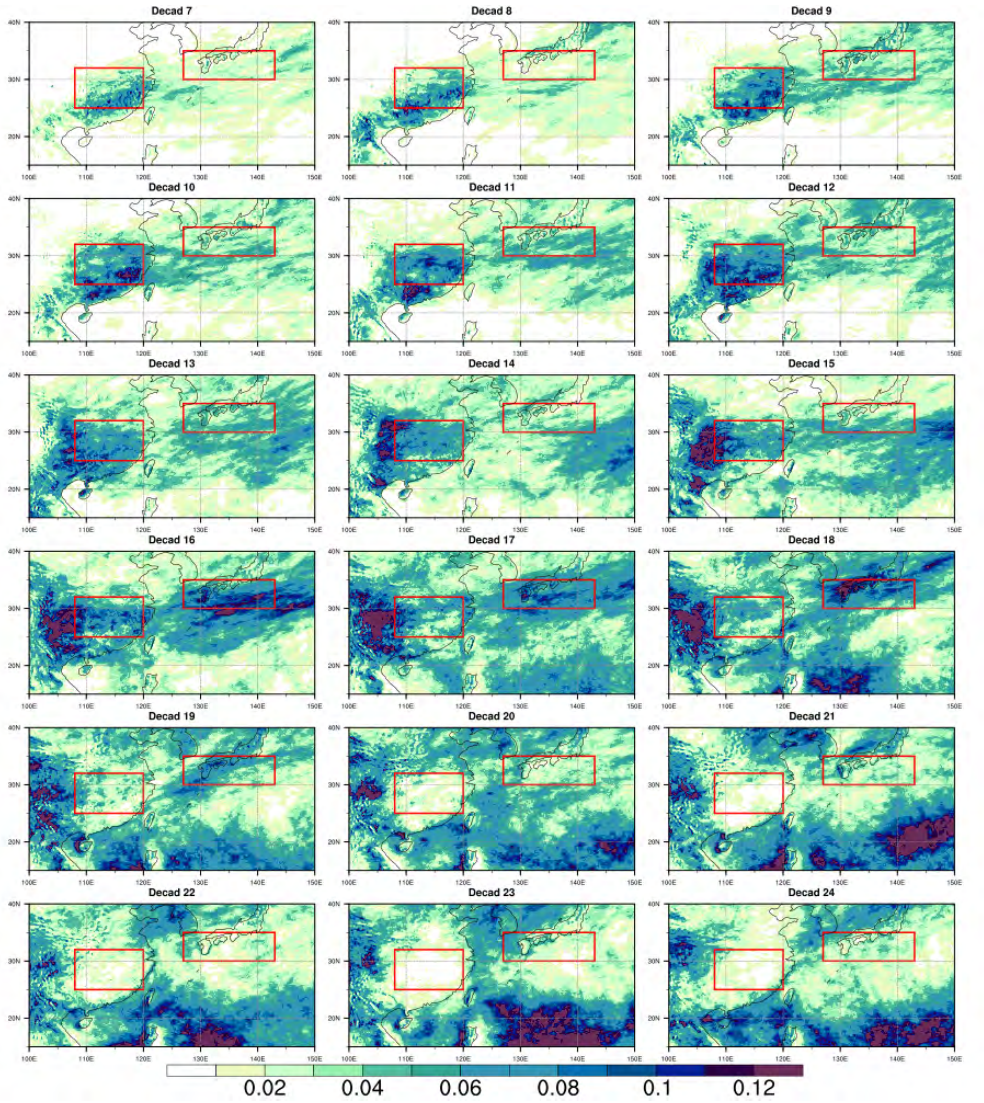

Fig. 3.5: As in Fig. 3.3, but based on MRI-AGCM3.2S simulation for the 1979-2003 period.

Figs 3.6 show the difference between climatological decad-mean and annual-mean probability of occurrence of extreme cases over two regions. It can be seen that the occurrence probability of extremes over EC is high from 11th to 21st decad, with a sharp peak in 17th to 18th decads (Fig. 3.6a). The model-simulated extremes tend to occur from 7th to 18th decads, with a relatively broad peak from 10th to 16th decad (Fig. 3.6c). It is probably due to the overestimation of springtime rainfall in the EC region. For the Bu region, both observations and simulations indicate a sharp peak from 16th

to 19th decad, followed by a secondary peak around 25th to 28th decad (Fig. 3.6b and 3.6d). Accordingly, the present climate simulation generally matches the current understanding that most of the heavy precipitation events occurs cocurrently with the northward passage of the Meiyu-Baiu rainband from June to mid-July. Due to model's capability of capturing realistic extreme activity in June to mid-July (1 June to 15 July), this period, referred to as the Meiyu-Baiu season, is focused on in this study. Hereafter, extreme precipitation cases are identified during wet days from June to mid-July only, so that all the rainfall extremes fall within the Meiyu-Baiu season. (The peak of extreme activity over Bu region occurs slightly later in the future-climate simulations, but it is still within the June to mid-July period.)

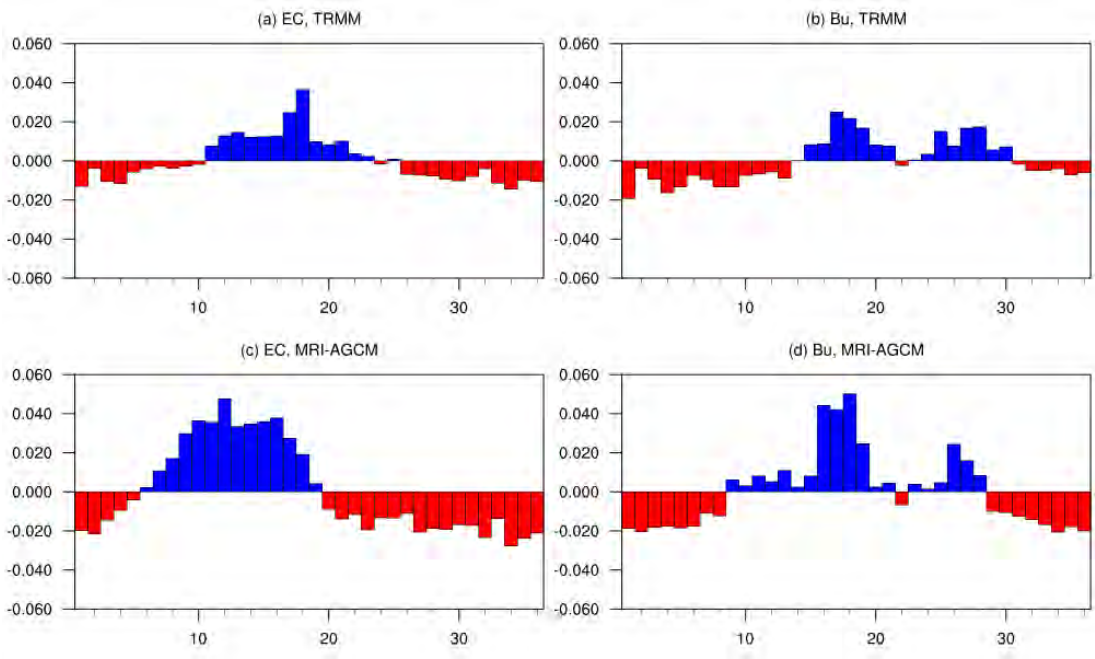

Fig. 3.6: Climatological decad-mean minus annual-mean probability of occurrence of extreme cases averaged over (a, c) Eastern China (25-32N, 108-120E) and (b, d) Baiu rainband (30-35N, 127-143E), based on (a, b) TRMM3B42v7 for the 1998-2013 period and (c, d) MRI-AGCM3.2S simulations for the 1979-2003 period, respectively.

Besides examining model's ability in capturing the timing of extreme cases, it is also important to compare the model-simulated intensity of Meiyu-Baiu extremes with observations. Fig. 3.7 gives the simulated 95th percentile (R95p) for the Meiyu-Baiu season (June to mid-July), as well as from those for TRMM and APHRODITE. The model can well capture the pattern of R95p from south Asia to east Asia (Fig. 3.7c), evidenced by comparison with both observational datasets (Fig. 3.7a and 3.7b). The simulated magnitudes of R95p are generally close to those based on APHRODITE, but are weaker than TRMM. Such deviation is probably due to the overestimation of heavy precipitation over southeastern China based on the TRMM dataset (Zhao and Yatagai, 2014).

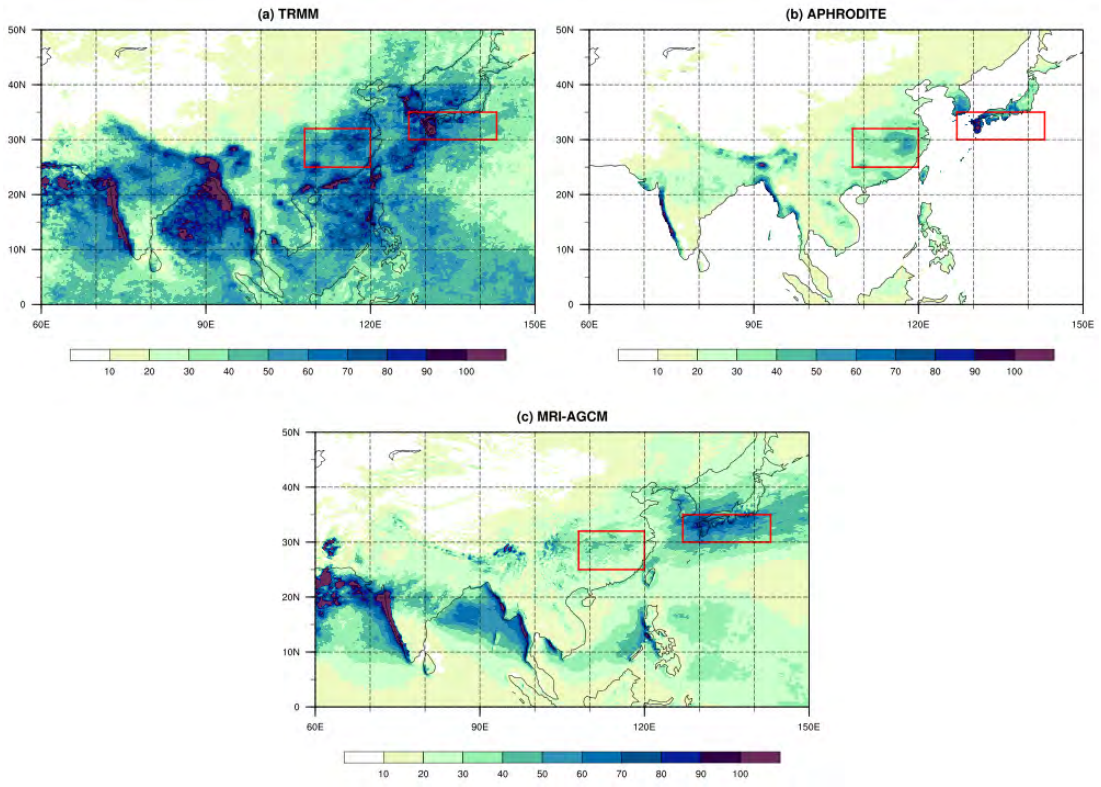

Fig. 3.7: R95p (units: mm day^{-1}) for June-to-mid-July computed based on (a) TRMM3B42v7 for the 1998-2013 period, (b) APHRODITEv1101, and (c) MRI-AGCM3.2S for the 1979-2003 period. The R95p is computed over land area only for APHRODITEv1101.

4. Methodology

4.1. Time filtering

In this study, emphasis is put on how global warming affects variations of Meiyu-Baiu extreme rainfall and its associated mid-latitude synoptic-scale systems based on model projections. As mentioned before, those weather systems are generated from the interaction between upper-level wave disturbances and surface baroclinity. It then forms a strong basis to use upper-level wave disturbances to indicate those mid-latitude synoptic-scale systems. According to Chang (1993), the anomaly of meridional velocity at 300 hPa (v300') is more likely to be dominated by smaller-scale systems and thus has better performance in describing synoptic-scale waves, compared to geopotential height at 500 hPa. Therefore, in the subsequent parts, v300' signal are used to represent upper-level transient waves, similarly to the method used by Chang and Yu (1999).

There exist some commonly used time filtering techniques to calculate anomalies. Bandpass filtering is one frequently used technique in filtering temporal signals, especially for those related to different timescales of wave. However, bandpass filtering will remove signal that are beyond the specified frequency band, which can alter the temporal evolution of characteristics of waves (Chang, 1993; Berbery and Vera, 1996; Chang and Yu, 1999). Trenberth (1991) found that the distortion caused by bandpass filtering may even impose more complexity in the interpretation of the result. In order to avoid those potential problems in explaining the result, hereafter, the anomalous signal is defined simply as the value of a variable after removal of its June-to-mid-July mean. Note that the anomalous field is calculated for each year, so as to remove the interannual variability of the seasonal mean. Anomalies

of different variables will be used to represent various features of transient weather systems.

4.2. Linkage between regional precipitation and upper-level disturbances

Before we associate upper-level disturbances with the extreme cases, their statistical relationship has to be examined first. 32 boxes are designed to find out statistical relationship between v300' over larger domain and daily precipitation anomaly (pp') within respective region. Fig. 4.1 shows the position of 32 boxes (with size of 5° × 5°) used to examine such statistical relationship. There are more boxes to the northwest of the center of the respective region, based on the assumption that influences of up-stream latitude travelling wave signals are stronger. From Fig. 4.2, it can be seen that there generally exists negative slope of regression line to the northwest and the east of EC region, while there exists greater positive slope over and to the north or northeast of EC region. Such zonally alternate sign of slope indicates the influence of certain upper-level synoptic-scale structure tilting to the northeast. In other words, positive anomalous precipitation in the region tends to occur when there exists an upper-level synoptic-scale wave pattern with the positive v300' signal influencing the region. Furthermore, it can be seen that the regression line in the south of 28.5N (the latitude of the center of EC region) shows much weaker slope than those in the north of 28.5N. It implies that the synoptic-scale wave structure is more likely coming from the mid-latitudes than from the tropics. A very similar pattern of those statistical relationships is found for Bu region (Fig. 4.3). Therefore, the regional average of precipitation for both regions are likely to occur within certain upper-level synoptic-scale patterns in the mid-latitudes.

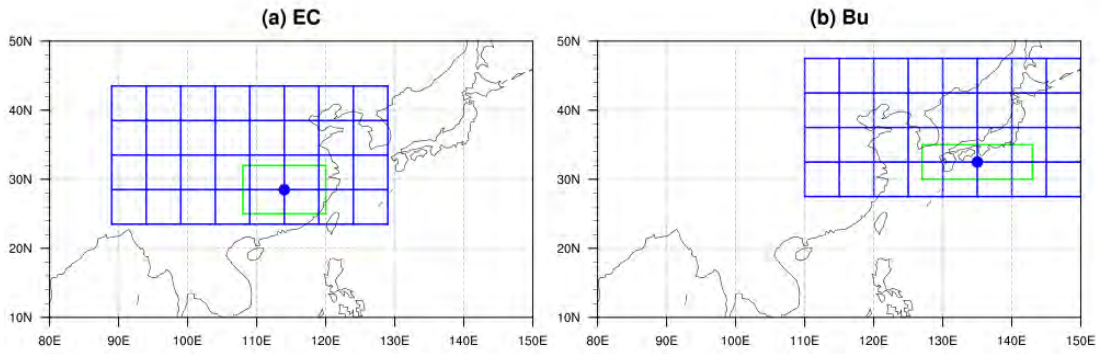

Fig. 4.1: 32 boxes used to examine statistical relationship between upper-level waviness and surface precipitation for (a) Eastern China (25-32N, 108-120E) and (b) Baiu rainband (30-35N, 127-143E). The blue dot, which is located at the interception point of boundaries of four nearest boxes, represents the center of (a) Eastern China (25-32N, 108-120E) and (b) Baiu rainband (30-35N, 127-143E) respectively.

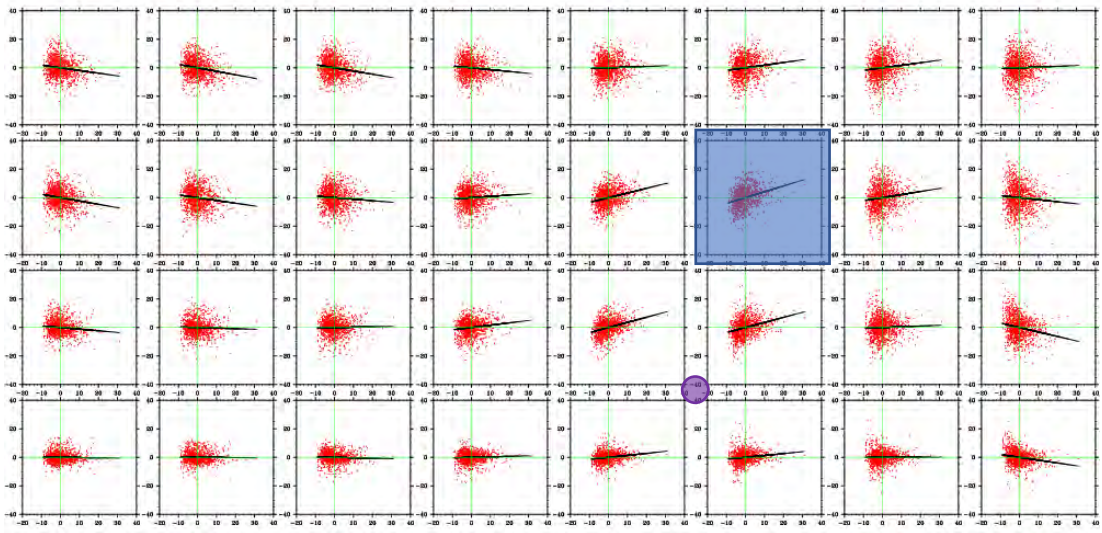

Fig. 4.2: Scatter diagrams showing the relationship between box-average v300' (units: m s^{-1}) and regional average pp' (units: mm day^{-1}) over Eastern China (25-32N, 108-120E). The position of purple dot and the arrangement of the panels corresponds to the location of the center of Eastern China and the spatial arrangement of boxes respectively as shown in Fig. 4.1a. The black line represents linear regression line between such two variables. The blue-shaded panel indicates that its regression line has the greatest slope among the regression lines of all panels. All the variables and regression lines are computed based on MRI-AGCM3.2S outputs from June to mid-July for the 1979-2003 period.

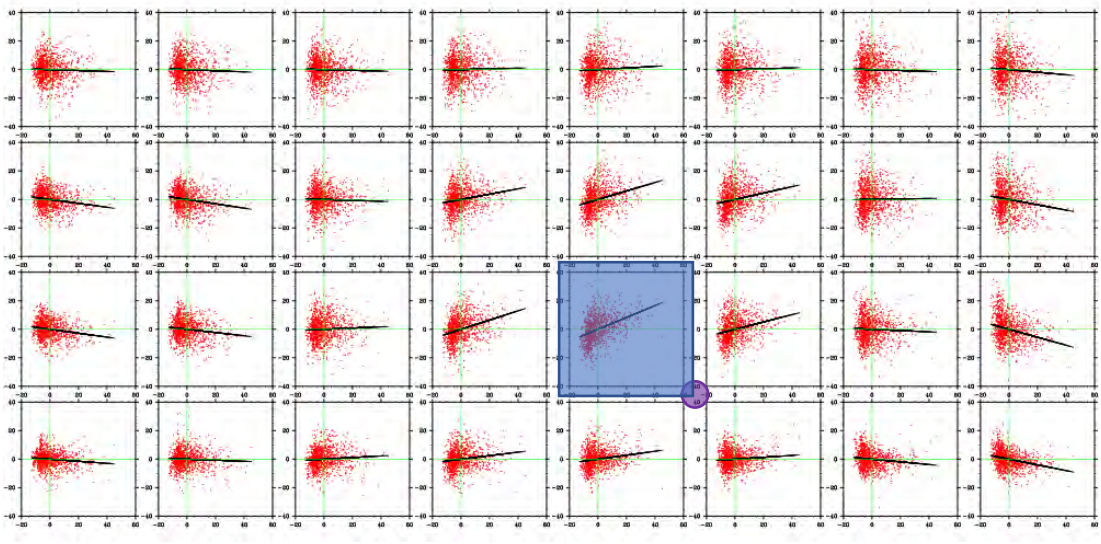

Fig. 4.3: As in Fig. 4.2, but based on regional average pp' over Baiu rainband (30-35N, 127-143E), the location of the center of the Baiu rainband and the spatial arrangement of boxes as shown in Fig. 4.1b.

By selecting the box in which the slope of linear regression line is the greatest (see Figs. 4.2 and 4.3), the relationship between its box-average v300' signal and the regional average pp' over the two regions is examined. It can be seen that the regression line for both regions exhibits a strong positive slope, but both the positive v300' and pp' signals are generally stronger for the Bu region than those for the EC region. Such findings imply that stronger upper-level v300' signals are related to stronger rainfall, especially for the Bu region. In other words, stronger positive upper-level v300' signals at particular location are likely to be associated with more extreme rainfall within each of the regions.

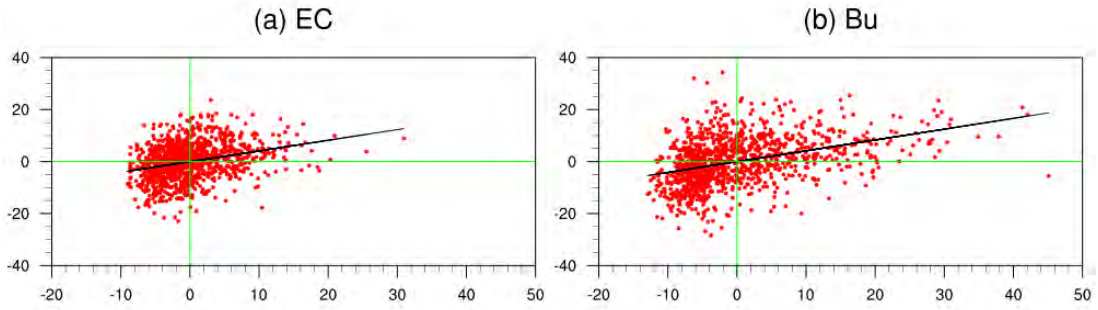

Fig. 4.4: Scatter diagrams showing the relationship between box-average v300' (units: m s^{-1}) and regional average pp' (units: mm day^{-1}) over (a) Eastern China (25-32N, 108-120E) and (b) Baiu rainband (30-35N, 127-143E). The box-average v300' is calculated in the most sensitive box, which is indicated as the blue-shaded panel in (a) Fig. 4.2 for Eastern China and (b) Fig. 4.3 for Baiu rainband respectively. The black line represents linear regression line between such two variables. All the variables and regression lines are based on MRI-AGCM3.2S outputs from June to mid-July for the 1979-2003 period.

4.3. Removal of TC-related extreme cases

In order to focus on the mid-latitude synoptic-scale systems, all the extreme cases related to tropical cyclones have to be removed first. Here, we will follow the detection algorithm for tropical cyclones used by Murakami et al. (2012). It includes criteria for 6-hourly model outputs, and some of which were optimized for the AGCM outputs to generate more realistic TC number. The criteria of the detection algorithm are shown below:

1) The maximum relative vorticity at 850 hPa exceeds 2.0×10^{-4} s^{-1}.
2) The maximum wind speed at 850 hPa exceeds 17.0 m s^{-1}.
3) The sum of temperature deviations at 300, 500, and 700 hPa exceeds 2.0 K, where the deviation is defined as difference between the maximum temperature and the average temperature over the 10°×10° box centered at the location of maximum vorticity at 850 hPa.
4) The maximum wind speed at 300 hPa is smaller than that at 850 hPa.

5) The genesis must occur over the ocean, and the duration of the system must be 36 hours or more. (Genesis is defined as the first detection of a system, with the exception at the boundaries of the study domain.)

After detection of tropical cyclones in the AGCM outputs, daily extreme cases are further classified into TC-related extreme cases (TC related) and non-TC related extreme cases (non-TC related). According to the distance threshold used by Jiang and Zipser (2010), an extreme case is considered as TC related if the distance between the case location and a TC center is smaller than 500 km at any synoptic hour. All the other cases are then considered as non-TC cases, which would be examined in the rest of this study.

4.4. Time composite

For non-TC related extreme rainfall cases, composite maps are computed to obtain the circulation associated with the synoptic-scale waves. Here, composite maps of v300’ and wind anomaly at 850 hPa (wind850’) are plotted for extreme rain days (defined as days in which at least one non-TC related extreme rainfall case is found within the search region). From Figs. 4.5a and 4.5b, it can be seen that significantly positive v300’ signals lie in both regions, with two negative v300’ signals found in both upstream and downstream positions. It indicates that an upper-level trough in the northwest of the region is likely to be associated with the extreme precipitation within the search region, consistent with the regression patterns shown in Figs. 4.2 and 4.3. Moreover, the composite maps also suggest the presence of synoptic-scale disturbances. From Figs. 4.5c and 4.5d, southwesterly monsoon basically extends from the Indochina Peninsula and South China sea, to the south of Japan. In the south (northwest) of the EC region, there exists anomalous low-level southwesterlies

(northeasterlies). The elongated zone separating these two opposite anomalous flows is orientated from west-southwest to east-northeast within EC region, resulting in a low-level shear-line characterized by such horizontal wind shear. Compared to those for EC region, the low-level circulation for Bu region is even stronger and larger. The corresponding anomalous wind flows resemble a typical mid-latitude cyclonic flow, whose center is located just south of Korea over the Korea-Strait. All the above findings suggest that the non-TC related extreme rainfall cases over both regions are likely to be associated with those synoptic patterns in the upper and low levels.

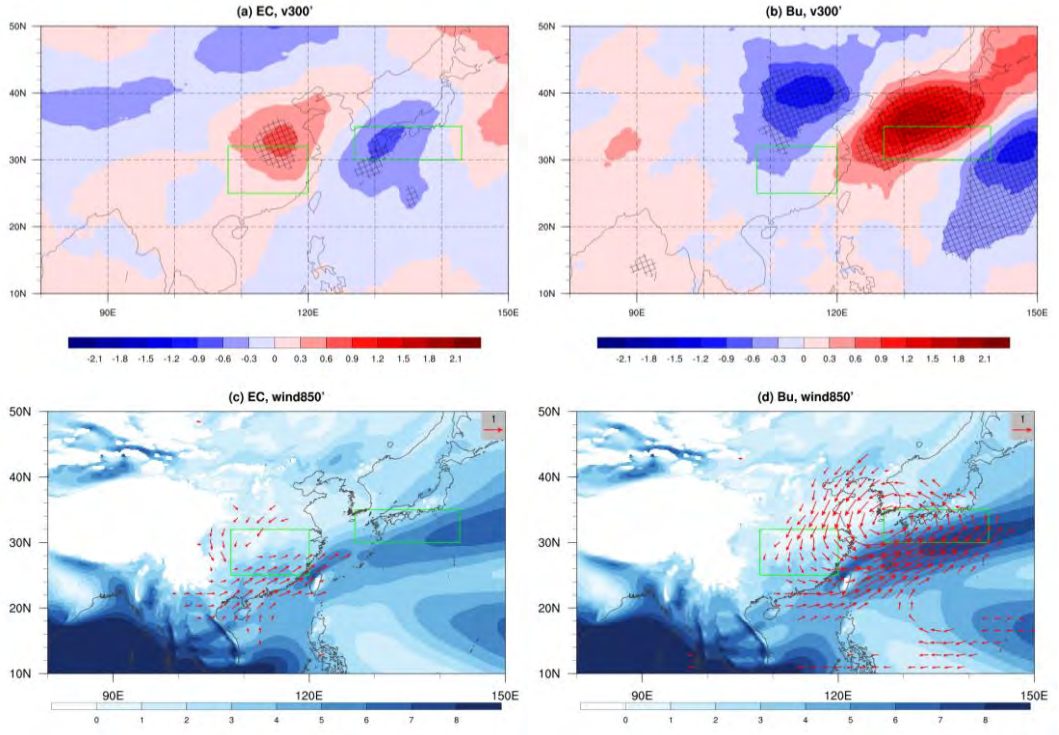

Fig. 4.5: Composite map of v300' (shading; units: m s^{-1}) for extreme rainfall days over (a) Eastern China (25-32N, 108-120E) and (b) Baiu rainband (30-35N, 127-143E), based on MRI-AGCM3.2S outputs from June to mid-July for the 1979-2003 period. Cross-hatches in (a) and (b) indicate that the anomalies are statistically significant at the 90% confidence level or above according to the two-sided student's t test. (c) and (d) as in (a) and (b), but for wind850' (see scale arrow at top right) and speed of wind850 (shading; units: m s^{-1}). Arrows for wind850' are drawn only if either zonal or meridional component of the wind850' is statistically significant at the 90% confidence level or above according to the two-sided student's t test.

Besides the spatial patterns of waves obtained from the composite maps, the phase speed of the upper-level wave can also be estimated by extending the time composites before and after extreme rainfall days. Although such kind of estimation may not accurately reflect the average phase speed of waves since the position of upper-level wave signals may vary from day to day, the existence of eastward propagating patterns of positive and negative signals in the composites can only be explained by upper-level traveling waves. Here, 6-hourly anomaly of meridional velocity at 300 hPa ($v300_{6hr}$') is used to enhance the temporal resolution. As indicated by the position of maximum positive v300' signal in Figs. 4.5a and 4.5b, mean $v300_{6hr}$' signal over latitudinal band of 31-36N and 33-38N for EC and Bu region respectively is considered. By finding the position of mean maximum positive $v300_{6hr}$' signal at different synoptic hour (from one day before to one day after the extreme rainfall days; figures not shown), the mean moving speed are estimated to be 6.5° and 5.0° eastward per day for waves influencing EC and Bu region, respectively.

4.5. Wave selection

4.5.1. Algorithm

Based on the characteristics of upper-level waves as shown in the previous composite plots, a novel wave-selection algorithm is developed to identify upper-level synoptic-scale waves associated with each non-TC related extreme rainfall case. Since those extreme rainfall cases may occur at different grid points on different days, it is very difficult to associate upper-level travelling waves to those cases simply by commonly used statistical methods such as empirical orthogonal function analysis. Here, the main idea is to ensure that there exists an eastward propagating wave-like v300' signal associated to the extreme rainfall cases. Therefore, a rectangular selection

domain, which is located in a certain position relative to the extreme rainfall case location, is used to check the existence of upper-level wave signal if some characteristics of travelling wave can be identified. A schematic diagram of the novel wave-selection algorithm is shown in Fig. 4.6.

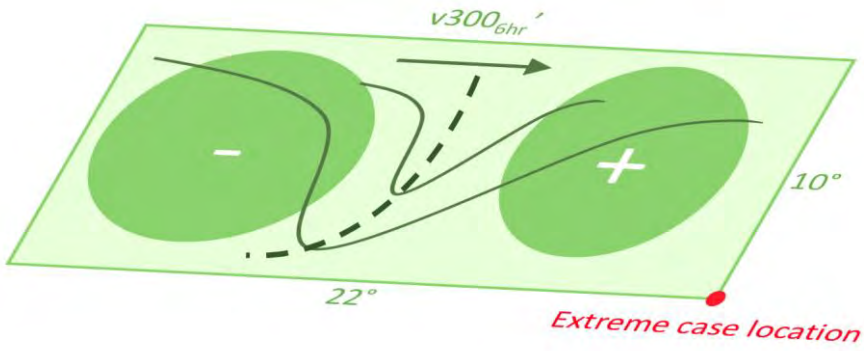

Fig. 4.6: Schematic diagram of the novel wave-selection algorithm. See text for details.

The first step of the wave-selection algorithm is to design a rectangular selection domain based on the understanding of short waves. As shown in the previous figures, non-TC related extreme rainfall cases are likely to be associated with a trough to the west of the search region. This algorithm thus tries to search for an upper-level travelling trough that might influence the surface precipitation. The main advantage of checking the existence of eastward travelling trough instead of wavy signals is that only part of the wave is required. Moreover, the travelling trough itself guarantees the synoptic-scale nature of the system and can be easily identified. Based on inspection of the previous composite maps (Figs. 4.5a and 4.5b), the wavelength of the upper-level wave patterns is found to be about 45°. The longitudinal extent of selection domain is then taken to be 22° (roughly half of the inspected wavelength), so that at most one trough can be captured within the selection domain for any wave of wavelength greater than 22°. The meridional width of the selection domain is set to be

10°, which is also determined by inspection of the main v300' signals in Figs. 4.5a and 4.5b. As shown in Fig. 4.6, the selection domain is located in the northwest (NW) quadrant of extreme case location, with its southeast corner positioned exactly at the case location. The reason why the NW position is chosen will be further explained later.

To ensure the dimension of the selection domain is suitable to capture most of the mid-latitude short wave, we further examine on the wave spectrum by applying zonal Fourier analysis of v300' signal over 60-150E from June to mid-July. From Fig. 4.7, it can be seen that the wave with wavelength (λ) of 45° has the largest amplitude and explains the greatest percentage variance among the first six dominant modes on average. It indicates that the patterns obtained from time composites in Figs. 4.5a and 4.5b in fact correspond to those of most dominant mode. The second dominant mode corresponds to the long wave of λ = 90°, but it will be neglected if the wave-selection algorithm is applied. The following two dominant signals are λ = 30° and λ = 22.5°, which are still greater than the designed longitudinal extent (22°) of rectangular selection domain. In general, the design of the rectangular selection domain is general enough to capture troughs associated with the three most dominant short waves (with wavelength of 22.5° to 45°). On the other hand, the most dominant short wave (λ = 45°) has the strongest amplitude and greatest variance within a relatively narrow band between 30-40N. It indicates that the main wave signals influencing precipitation over the search regions tend to be the strongest within a relatively small latitudinal band. Therefore, the meridional width of rectangular selection domain (10°) is able to identify at least the strong signals of the most dominant waves.

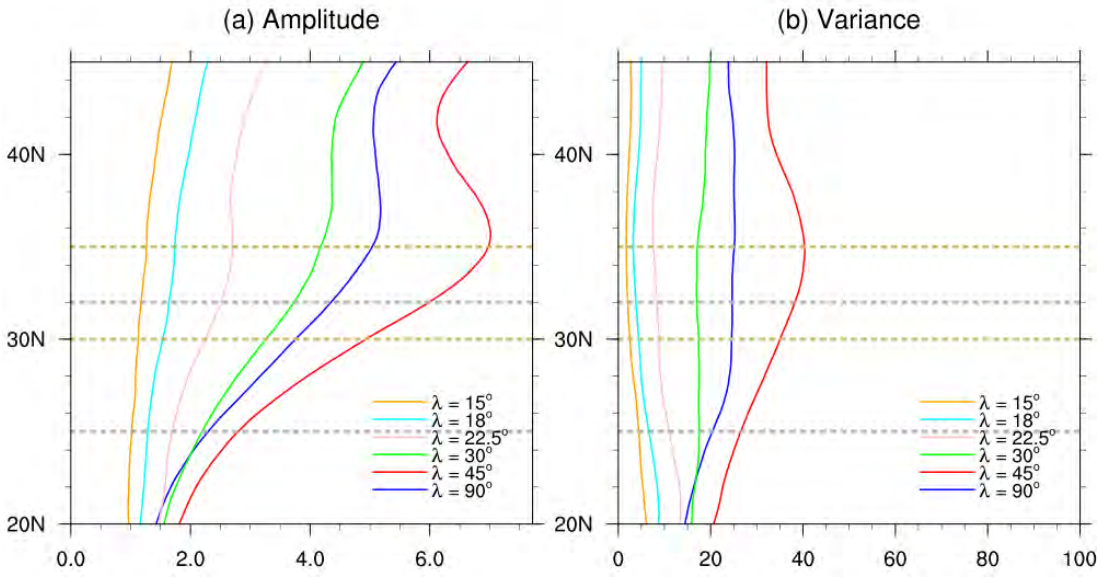

Fig. 4.7: (a) Average amplitude (units: m s^{-1}) and (b) average variance (units: %) of first six dominant wavelengths (λ) from daily zonal Fourier analysis of v300' within 60-150E, based on the MRI-AGCM3.2S outputs from June to mid-July for the 1979-2003 period. The grey and golden horizontal dashed lines represent the meridional boundaries of Eastern China (25-32N, 108-120E) and Baiu rainband (30-35N, 127-143E) respectively.

Three criteria are then designed to examine whether an upper-level travelling trough exists within the selection domain. The criteria of wave-selection algorithm are shown below:

<u>At any synoptic hours (00, 06, 12, 18UTC):</u>

1) At least 25 % of area of selection domain gives positive $v300_{6hr}$', and at least 25 % gives negative $v300_{6hr}$'.
2) Mean longitude of positive $v300_{6hr}$' is larger than that of negative $v300_{6hr}$' by at least 5.5°.

<u>Changes from 00UTC to 18UTC:</u>

3) Change of $v300_{6hr}$' from positive to negative, over at least 11 (9) % of area of selection domain for EC (Bu) region

The first criterion requires that there is a minimum fraction of area for both negative and positive $v300_{6hr}$' signals in the domain, which is consistent with the presence of an upper-level trough. Since the portion of area of either negative or positive signal is equal to 50 % in an idealized situation (a trough within a perfectly sinusoidal wave bisects the selection domain into an eastern half with positive and a western half with negative signals), the threshold of 25 % is used to accommodate for non-idealized situations. The second criterion then set up a requirement on the relative positions of the negative and positive $v300_{6hr}$' signals. Since the difference of mean longitude of signals in opposing signs within the domain is equal to 11° in the idealized situation, the threshold of 5.5° is used to allow some variations of the v300' pattern. Together, the first and second criteria are designed jointly to indicate the existence of an upper-level trough, at one of the synoptic hours. Some may argue that whether such two criteria can be simply replaced by examining vorticity instead. However, the signals based on upper-level vorticity exhibits more noise than those based on v300', which is probably due to better performance of v300' in describing synoptic-scale waves compared with other variable (Chang 1993). After identifying the upper-level trough, a third criterion is further applied to examine whether the trough signal is propagating eastward (and thus of synoptic scale). The threshold value 11 (9) % for EC (Bu) indicates the portion of area where $v300_{6hr}$' signals reverse their sign from positive to negative in one day. Since the estimated phase speed from the previous composites for the waves affecting EC (Bu) region is 6.5° (5.0°) eastward per day, the threshold value is calculated by considering half of such phase speed, so that majority of short propagating waves are expected to fulfil this criterion. In fact, a fourth criterion within an additional selection domain is also used to identify low-level southwesterlies (one kind of the synoptic-scale features of the wave systems as shown in Figs. 4.5c

and 4.5d). However, adding such low-level criterion hardly affect the results (which will be mentioned later). Therefore, both the selection domain and its criterion in the low level will be skipped hereafter.

By applying all three upper-level criteria, results due to different positioning of selection domain relative to the extreme case location are examined. Fig. 4.8 shows the nine locations of the domain relative to that of the extreme case. Here, the domain-average daily-mean value of $|v300_{6hr}'|$ is considered as a measure of wave activity within the selection domain. From Fig. 4.9, it can be seen that both the fraction of number of extreme rainfall cases satisfying all three criteria and the mean of the regional wave activity are the largest when the selection domain is NW of the extreme case location. Such fraction and wave activity drop rapidly for other boxes in the southward and eastward direction. Note that even stronger signals are found for the Bu region (see Fig. 4.10). All these findings provide strong basis for choosing the NW box for the wave-selection algorithm. Hereafter, wave-related extreme rainfall cases are identified as the extreme rainfall cases which satisfy all three criteria within the corresponding NW selection box, and wave-related extreme rainfall days are defined as the days in which at least one wave-related extreme rainfall case is found in the search region.

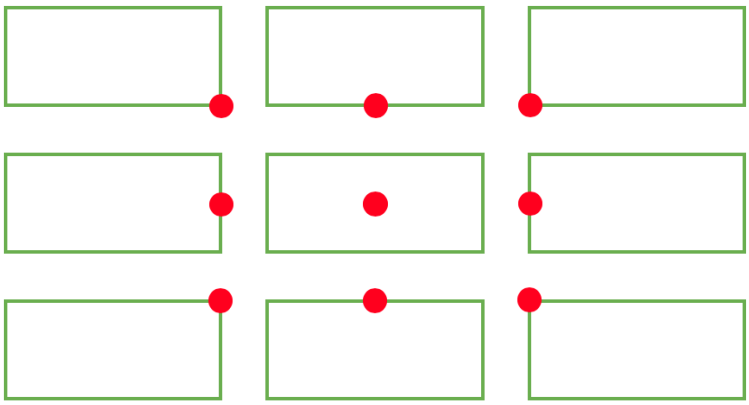

Fig. 4.8: A schematic diagram of nine locations of the selection domain (rectangle) relative to the extreme case location (red dot). There exists only one extreme rainfall case, but nine rectangles are drawn to indicate nine different ways of locating the selection domain relative to such case location. The top left (northwest) domain indicates that the extreme case is located at its bottom right (southeast) corner, the top middle domain indicates that the extreme case is located at the middle of its bottom (southern) edge, and so on.

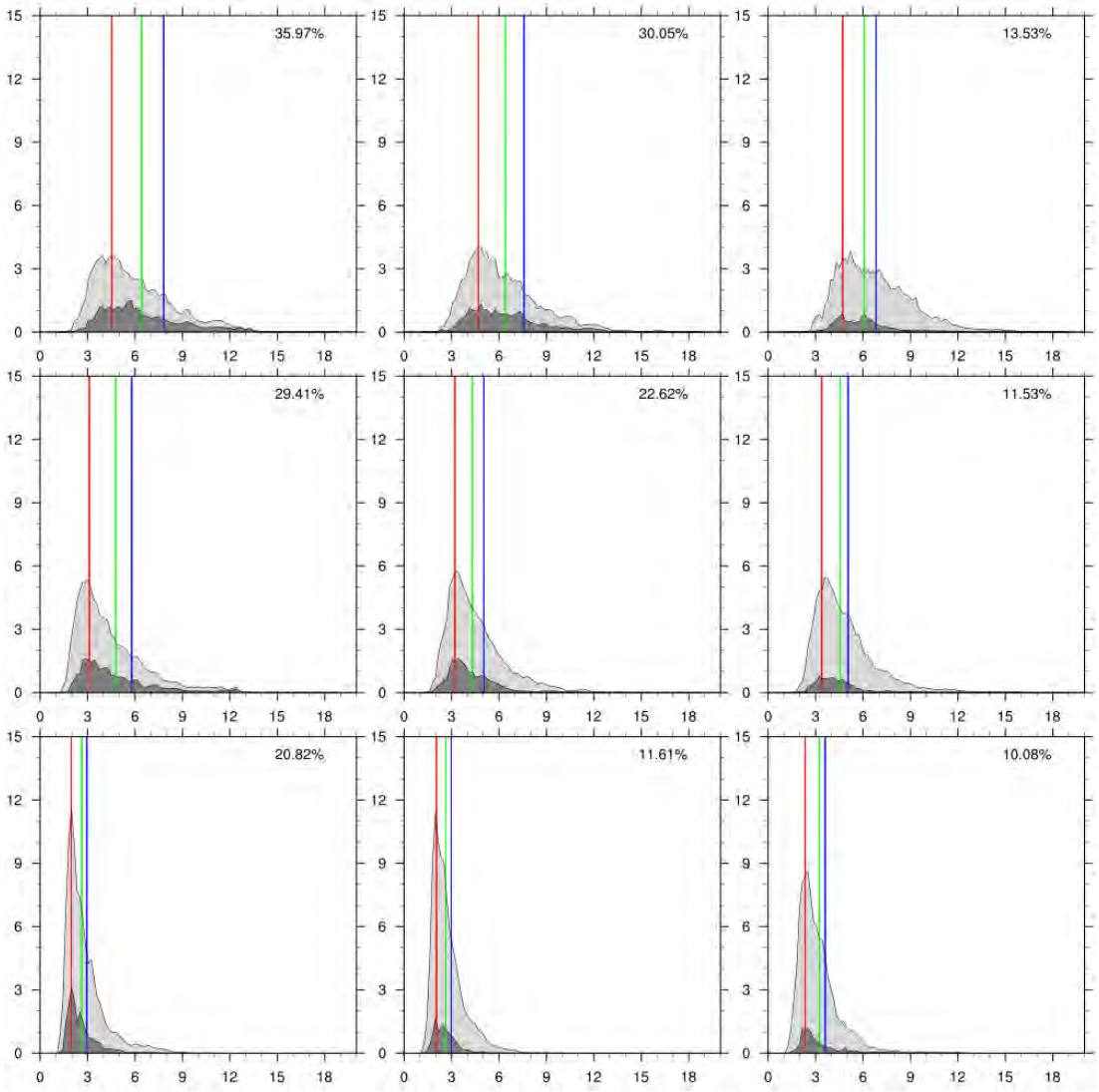

Fig. 4.9: Probability density function (units: %) of domain-average daily-mean value of $|v300_{6hr}'|$ (units: m s^{-1}) before (light grey shading) and after (dark grey shading) applying the three criteria in the selection domain, based on all non-TC related extreme rainfall cases over Eastern China (25-32N, 108-120E). The probability density function is computed based on 100 bins between the minimum and maximum values of $|v300_{6hr}'|$. The arrangement of the panels corresponds to the nine locations as shown in Fig. 4.8. The red, green and blue lines respectively represent the lower quartile, mean and upper quartile of domain-average daily-mean value of $|v300_{6hr}'|$ after applying the three criteria. The number at top right corner indicates the percentage of number of non-TC cases satisfying the three criteria. $v300_{6hr}'$ is computed based on the MRI-AGCM3.2S outputs from June to mid-July for the 1979-2003 period.

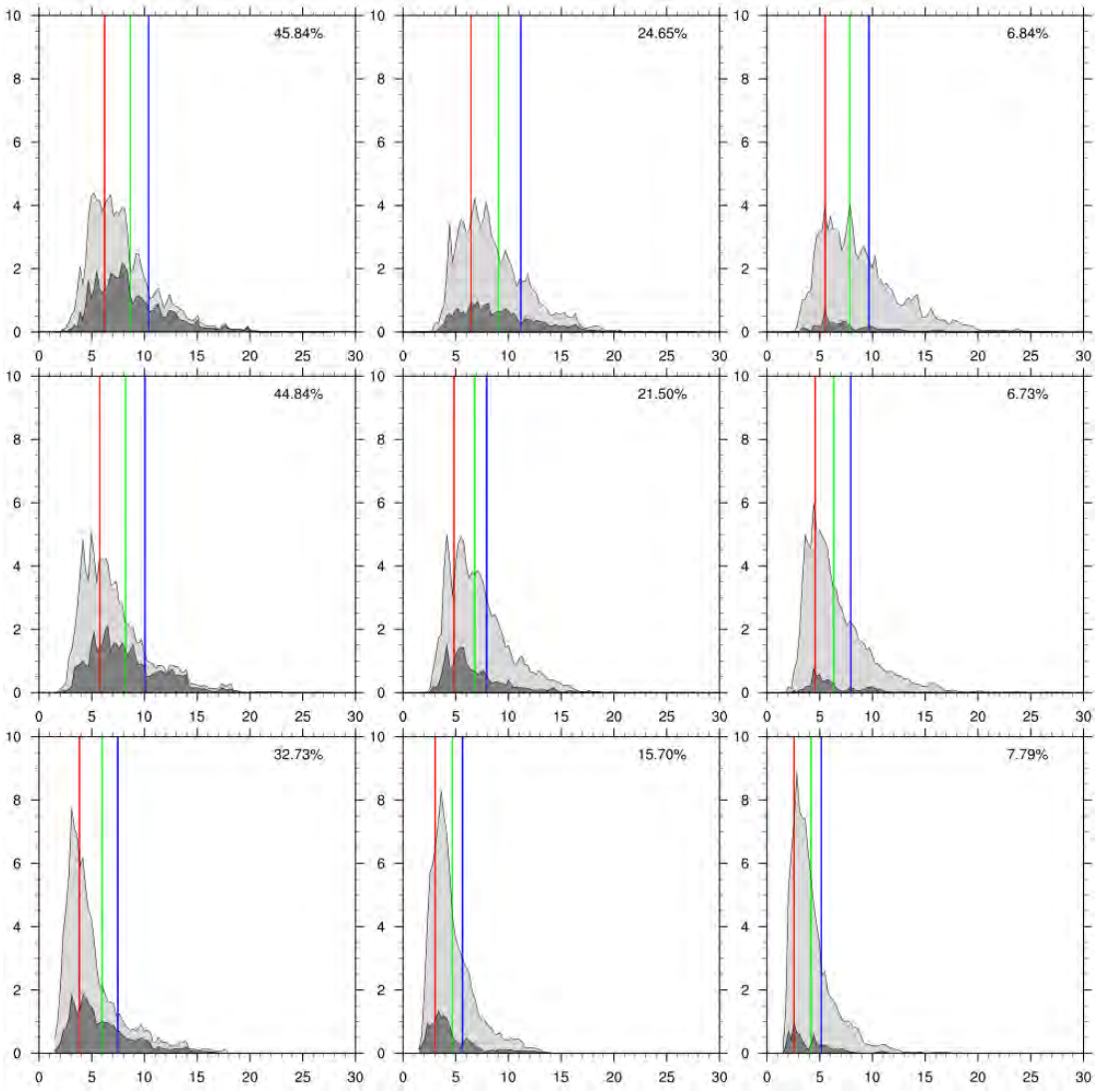

Fig. 4.10: As in Fig. 4.9, but based on non-TC related extreme rainfall cases over Baiu rainband (30-35N, 127-143E).

Sensitivity of the wave activity to the above wave-selection algorithm has to be examined in order to ensure the robustness of the results. Here, we examine the sensitivity of the wave activity to individual threshold value by adding ± 20% to each of threshold value keeping the others unchanged. Plots as in Figs 4.9 and 4.10 are drawn (not shown here) accordingly to see whether the optimal position of selection box and the domain-average wave signal is unchanged. Results show that the optimal selection box based on the greatest wave signal and the greatest proportion of cases

satisfying the three criteria is still in the NW position. The probability density function of domain-average wave signal within such NW box changes very slightly in its shape, and no obvious change of the lower quartile, mean and upper quartile is found. It is because the threshold values used in the first two criteria have been accommodated for non-idealized situations. Also, the third threshold value is taken as half of the estimated phase speed of wave signals, so that those signals are not expected to be strongly influenced by the threshold value. Moreover, since the change of phase speed of waves from the past to the future is found to be very small, using the same threshold value for the third criterion in the future-climate simulations does not directly affect the results. These findings guarantee low sensitivity of the results to the three threshold values used in the wave-selection algorithm. (In fact, nearly 90% or more cases satisfying these three criteria also satisfy the fourth criterion in the low-level selection domain under sensitivity test. Wave activities are almost unchanged after the addition of the fourth criterion.)

4.5.2. Clustering

Although wave-related extreme rainfall days can be identified by using such wave-selection algorithm, these days may be serially related, forming clusters spanning more than one day during which wave-related extreme rainfall is found in the search regions. To properly compute composite maps with temporal information, one needs to identify these clustered extreme rainfall days. Here, each group of consecutive wave-related extreme rainfall days is deemed as one cluster. A single isolated wave-related extreme rainfall day will also be considered as a cluster. To ensure the extreme rainfall cases within each cluster are relevant to the same upper-level trough signal, we further look at the average longitude of extreme rainfall case

locations at each day within each cluster. From Figs 4.11 and 4.12, we can see that the average longitude of extreme case locations within majority of clusters is increasing from day to day. However, the mean longitude drops abruptly within certain clusters, which is likely to be due to another trough coming immediately after departure of the original one. In order to ensure that each cluster is related to a single wave, in case that the average longitude drops more than 6° (8°) for EC (Bu) region (half of the longitudinal extent of search region) in consecutive days, such cluster would be further split into two clusters. After addition of this modification, the statistics of the adjusted clusters are shown in Fig. 4.13. From the figure, it can be seen that the duration of most of the adjusted clusters varies from 1 to 5 day, which is consistent with the temporal scale of a synoptic-scale system. There also exist very few adjusted clusters whose duration is more than 6 days, but those are likely to be influenced by travelling waves with relatively low phase speed.

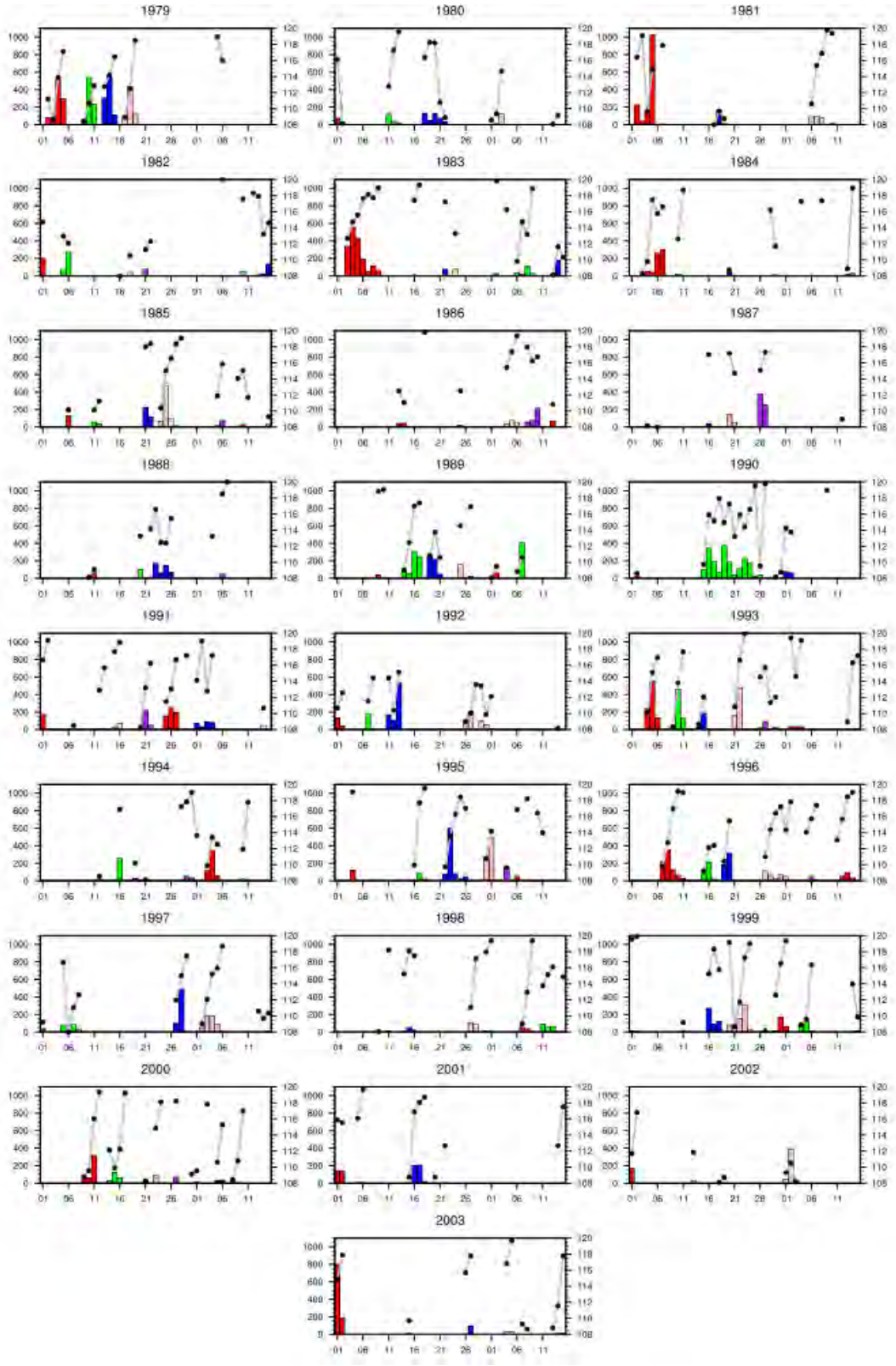

Fig. 4.11: Daily count of wave-related extreme rainfall cases (bars; left y-axis) over Eastern China (25-32N, 108-120E), based on the MRI-AGCM3.2S outputs from June to mid-July for the 1979-2003 period. Consecutive bars of the same color belong to the same cluster. Black dots, which are joint by a grey line within the same cluster, represent the average longitude of extreme case locations (right y-axis; units: degree east).

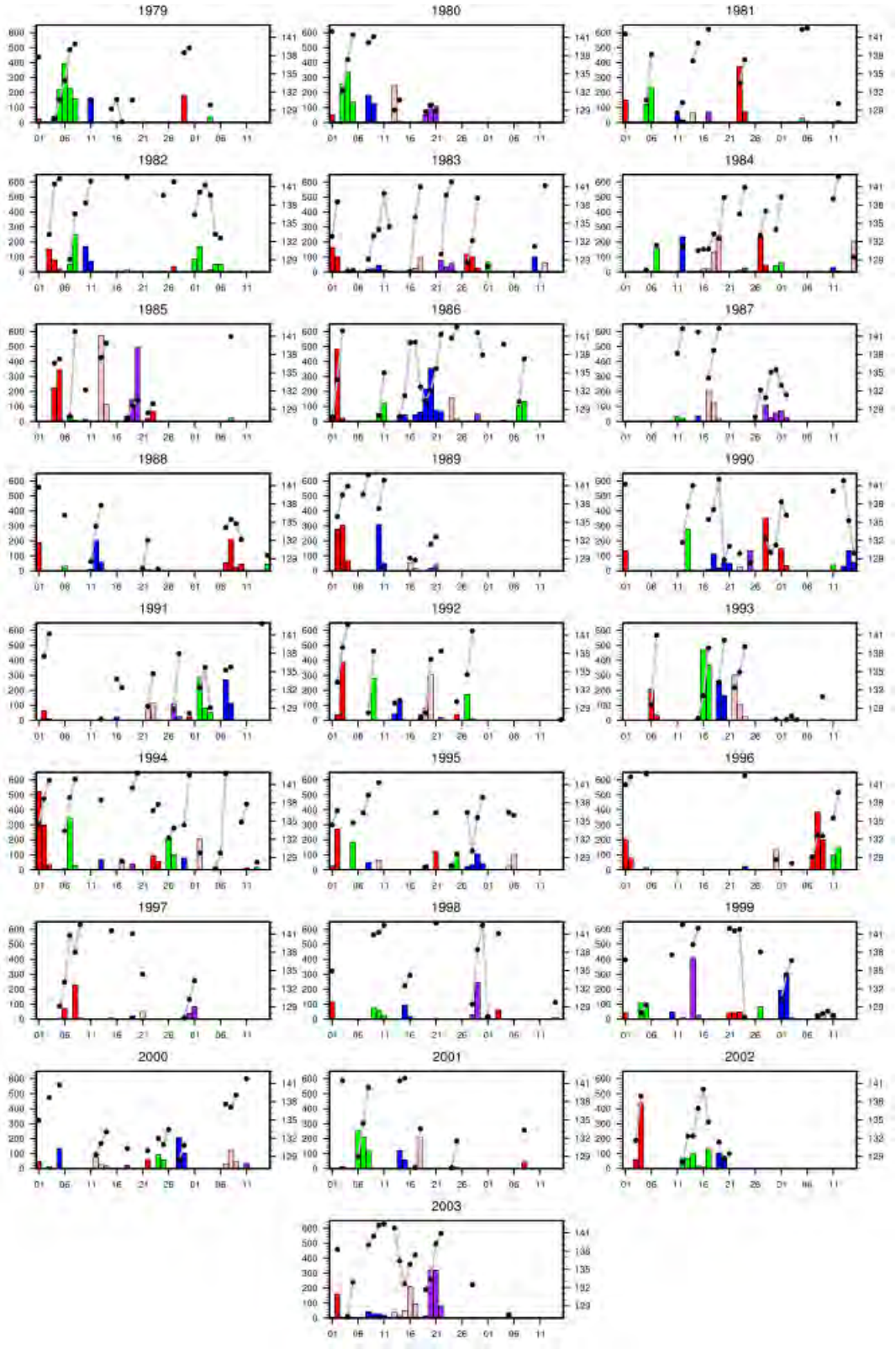

Fig. 4.12: As in Fig. 4.11, but for wave-related extreme rainfall cases over Baiu rainband (30-35N, 127-143E)

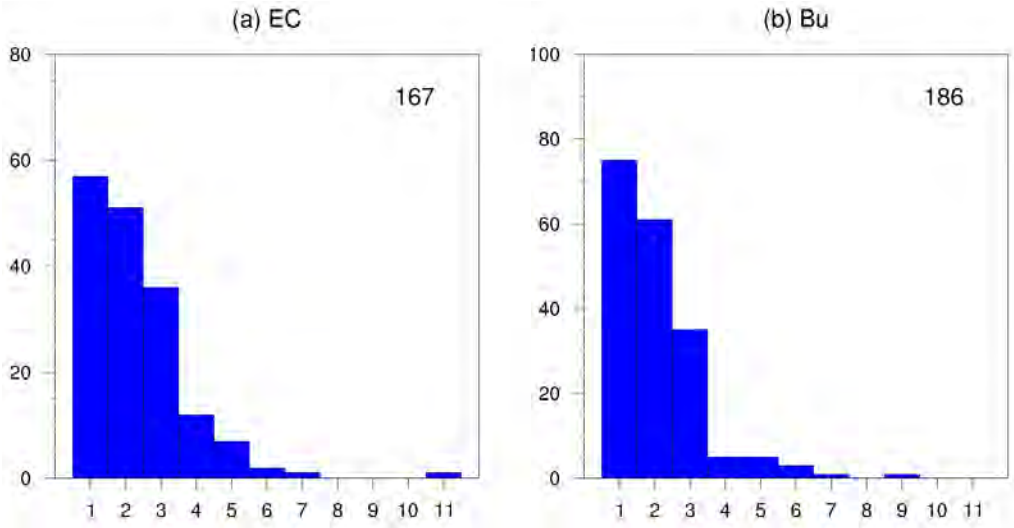

Fig. 4.13: Number of adjusted clusters with different duration time (units: day) over (a) Eastern China (25-32N, 108-120E) and (b) Baiu rainband (30-35N, 127-143E), based on the MRI-AGCM3.2S outputs from June to mid-July for the 1979-2003 period. The number at the top right corner indicates the total number of adjusted clusters.

It is important to identify the 'peak' day on which the wave brings the greatest influence on rainfall over the search region, so that composites can be computed properly. Here, the day on which the regional mean precipitation becomes maximum within each adjusted cluster is defined as day 0 (the cluster of one-day duration is directly defined as day 0). The results based on day 0, and also days from lag = -2 to lag = 2 (day -2 to day +2) will be analyzed in details in chapter 5.

4.5.3. Results based on observations and reanalysis

To ensure that the AGCM yields realistic results, we further apply the wave-selection algorithm (followed by the clustering technique) to observations and reanalysis data. For this purpose, both the ERA-interim reanalysis data and TRMM precipitation dataset over 1998-2013 period are first regridded to the same grids as those of the MRI-AGCM. Afterwards, non-TC related extreme rainfall cases from June to mid-July are identified based on the best track data from JTWC. Fig. 4.14

shows the composite maps computed from the corresponding extreme rainfall days. It can be seen that both the upper-level wave patterns and low-level circulation structure are very similar to those obtained in model simulations (Fig. 4.5). However, the model exhibits slight underestimation of the intensity of southwesterlies influencing both regions. After applying the wave-selection algorithm based on those information, wave-related extreme rainfall days are used to compute composite maps for day 0 (and also from day -2 to day +2). Results show that there exists general consistency in the pattern and also the phase speed of upper-level wave between model simulations and the observation/reanalysis datasets. The magnitude of mean wave signals is similar for the EC region, but the AGCM slightly overestimates those affecting the Bu region (figures not shown). In general, the wave-selection algorithm is demonstrated to generate realistic results by applying the same methodologies on the observations/reanalysis datasets. Afterwards, the algorithm using the same threshold values and for the NW selection box is then applied for the future climate simulations, so as to infer impacts of global warming on the extreme rainfall and the associated wave systems.

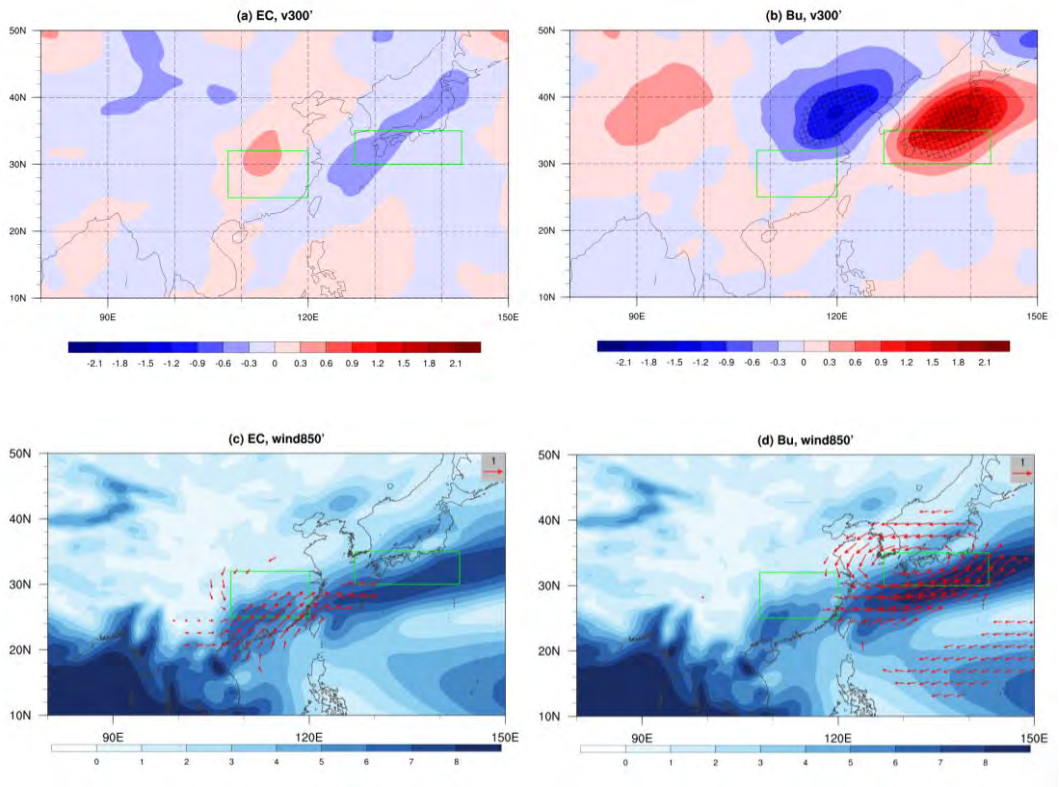

Fig. 4.14: As in Fig. 4.5, but based on ERA-interim reanalysis and TRMM3B42v7 precipitation dataset from June to mid-July for the 1998-2013 period. Both the reanalysis and precipitation dataset are regridded to the same grids as those of the MRI-AGCM3.2S before the composite maps are computed.

5. Projected changes of extreme rainfall and associated synoptic-scale systems

5.1. Extreme rainfall

The projected changes of different extreme rainfall indices over the main Asia and western north Pacific are first examined, before the associated synoptic-scale systems are investigated. Fig. 5.1 shows the projected changes of the Simple Daily Intensity Index (SDII; defined as daily rainfall averaged over wet days only) and R95p in the future-climate simulations. It can be seen that both of them are projected to increase significantly over most of the area within both EC and Bu regions. The projected change of the regional average of SDII and R95p indices are +1.6 (+4.9) and +2.0 (+9.5) mm day^{-1}, with percentage change between 15 to 17%, over the EC (Bu) region. There exists a broad latitudinal band (roughly between 90-150E and 20-35N) in which significantly positive change signals are found. Moreover, there are also two main bands of negative signals, one of which extends from the central China, Korea and around the northern Japan, and the other of which covers the south China sea and seas in the east of Philippines. Since large-scale atmospheric circulations over Asia and northwestern Pacific are often distributed alternately in different latitudinal bands, their projected changes may be related to those alternately opposite signals. In order to better understand their relationship, further analyses of the projected changes of synoptic-scale systems associated to non-TC related extreme rainfall cases, as well as the variation of background circulations over East Asia in the future, will be carried out.

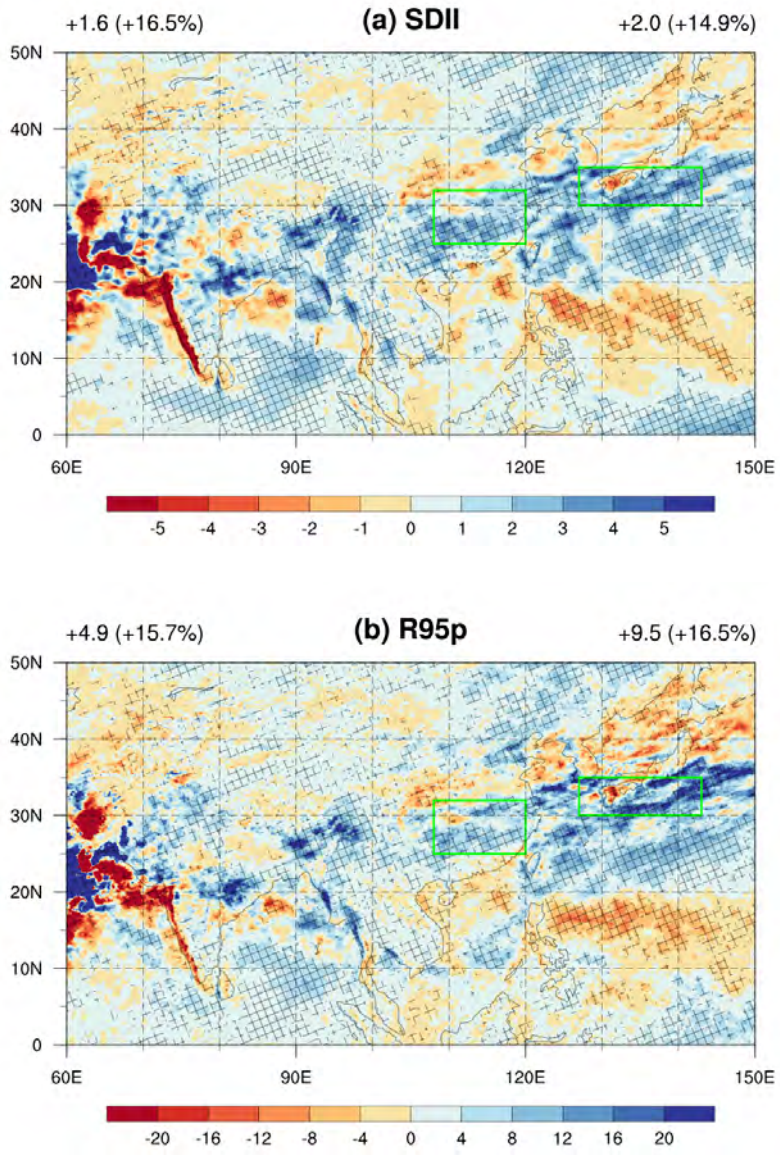

Fig. 5.1: Globally-warmed minus present-day (a) SDII (units: mm day^{-1}), and (b) R95p (units: mm day^{-1}) based on the MRI-AGCM3.2S outputs from June to mid-July. Their regional average values (and percentage changes) over the Eastern China (25-32N, 108-120E) and Baiu rainband (30-35N, 127-143E) are shown in the upper left and upper right corner respectively in each panel. Cross-hatches indicate that the differences are statistically significant at the 90% confidence level or above according to the two-sided Monte Carlo permutation test.

5.2. Associated synoptic-scale systems

5.2.1. Upper-level waves

The change of pattern of the associated upper-level wave signals under global warming is examined by computing composite maps of v300’ for day 0 in the present and future climate simulations. From Fig. 5.2, it can be clearly seen that there exists a wave train (within 30-45N) with wavelength of about 45° to 50° affecting the search regions, in both present and future climate simulations. Such a wave train is positioned in a way that, a significantly positive v300’ signal is influencing just up-stream of the search region, while negative signals are located to its east and west. Under the influence of global warming, the trough embedded in the upstream synoptic-scale wave seems to be shifted southward slightly, for both EC and Bu regions. The mean wave amplitude and anomalous streamfunction at 300 hPa (Ψ300’) shown in composite maps can also be used to roughly estimate the magnitude of these waves. Results show that while there is no obvious change for those affecting EC, the mean amplitude of waves influencing the Bu region exhibit weakening in the globally warmed future.

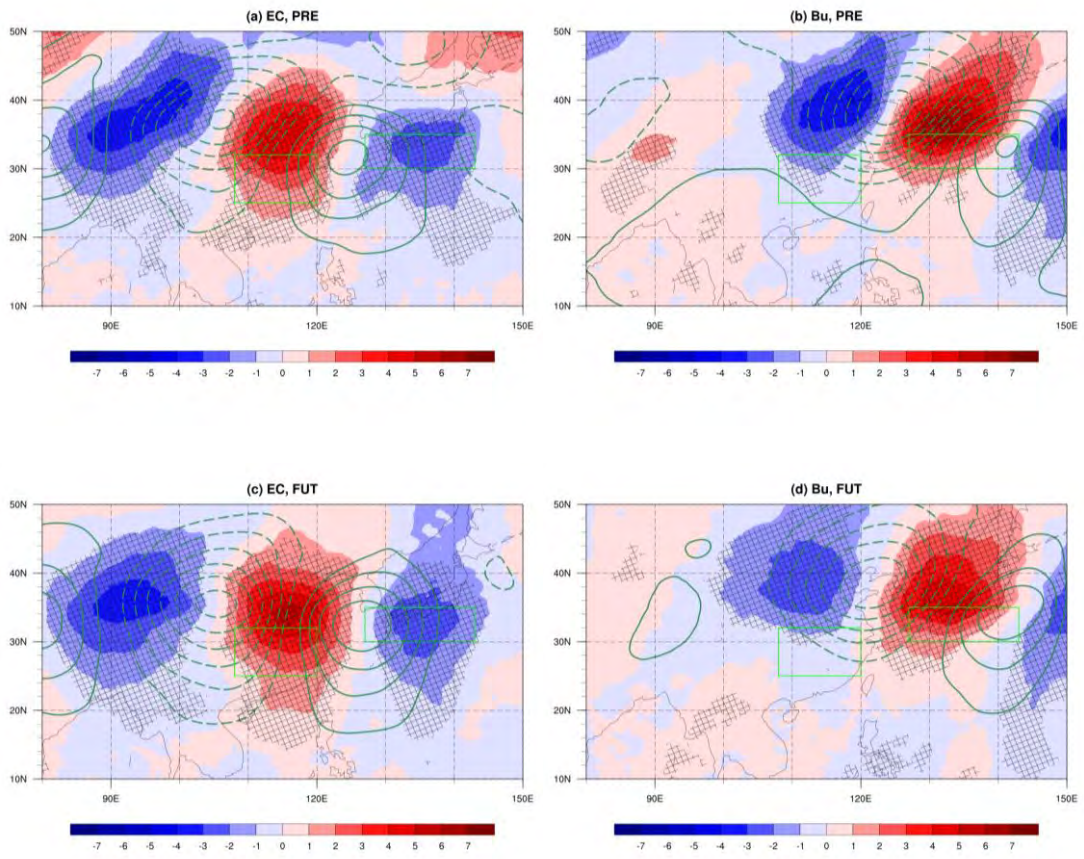

Fig. 5.2: Composite map of v300' (shading; units: m s^{-1}) and Ψ300' (contours in spacing of 2 × 10^6 m^2 s^{-1}) for day 0 over (a, c) Eastern China (25-32N, 108-120E) and (b, d) Baiu rainband (30-35N, 127-143E). They are computed based on MRI-AGCM3.2S outputs from June to mid-July, for the (a, b) present climate and the (c, d) future climate respectively. Dashed (solid) contours represent negative (positive) Ψ300', and the zero-line of Ψ300' is not drawn in the panels. Cross-hatches indicate that the v300' anomalies are statistically significant at the 90% confidence level or above according to the two-sided student's t test.

In addition to inspecting composite maps, here, we also examine the amplitude of individual v300' wave trains within a rectangular domain upstream of the EC and Bu regions. The northern (southern) boundary of such domain is the same as the northernmost (southernmost) boundary of rectangular selection domains for wave selection (see Chapter 4), while the western (eastern) boundary coincides with the longitudinal positions of the negative (positive) v300' signal associated with the embedded trough. The wave amplitude is then defined as the half of the difference

between the mean of maximum 5% of positive v300' and that for the minimum 5% of negative v300' within the domain. The probability density function of the wave amplitudes for day 0 are computed and shown in Fig. 5.3. It can be seen that the mean wave amplitude affecting both regions is projected to decrease by about 6% in the globally warmed future. The mean amplitude decrease of about 0.8 (1.0) m s^{-1} passes the 95% significance level based on one-sided Monte Carlo permutation test, for the EC (Bu) region. Such weakening can be explained by the shift of probability density function for intensity of those upper-level waves. It can be seen that for both regions, waves with weak-to-intermediate amplitude become more likely to occur, while the remaining strong waves generally decrease its occurrence probability in the future climate simulations.

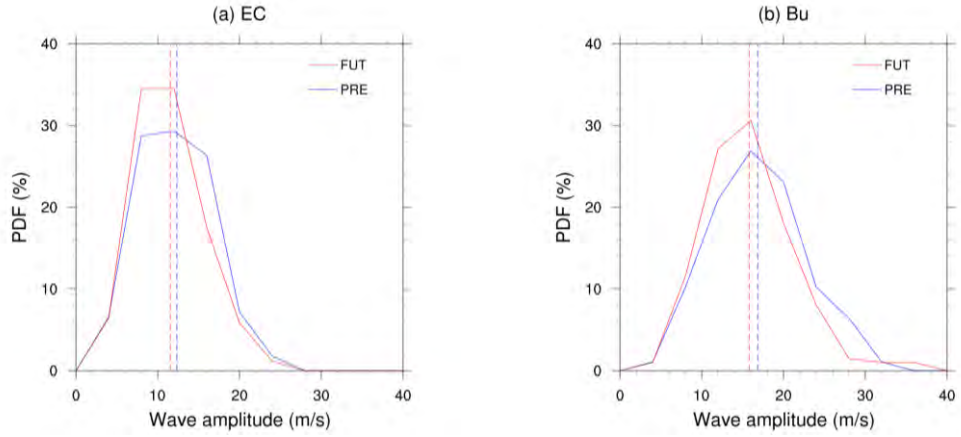

Fig. 5.3: Probability density function (units: %) of wave amplitude (units: m s^{-1}) for day 0 over (a) Eastern China (a) (25-32N, 108-120E) and (b) Baiu rainband (30-35N, 127-143E), based on MRI-AGCM3.2S outputs from June to mid-July for the present climate and the future climate respectively. The red (blue) dashed vertical line represents mean wave amplitude for the present (future climate)

Composite maps from day -2 to day +2 are also computed in order to examine on changes of the track of upper-level waves under a warmed climate. From Figs 5.4 and 5.5, it can be seen that wave trains influencing both regions propagate eastward

with nearly the same patterns (i.e. along the subtropical jet stream) in the future. However, the positive v300' signal area associated with the troughs affecting EC shifts southward slightly from day 0 to day +1 (Figs. 5.4e to 5.4h). The wave train for Bu region at day 0 also shows slightly southward shift, but the trough influencing Bu region weakens obviously in the future projections from day 0 to day + 2 (Figs. 5.5e to 5.5j). Such a slight southward shift in both regions is probably related to a similar shift of the climatological mean subtropical jet stream, particularly at northern Pakistan and the East China Sea. On the other hand, the climatological mean subtropical jet stream is found to intensify in the section from central China to Japan under the warmed future. However, there is no obvious change of phase speed of the wave trains influencing both regions in the globally warmed future.

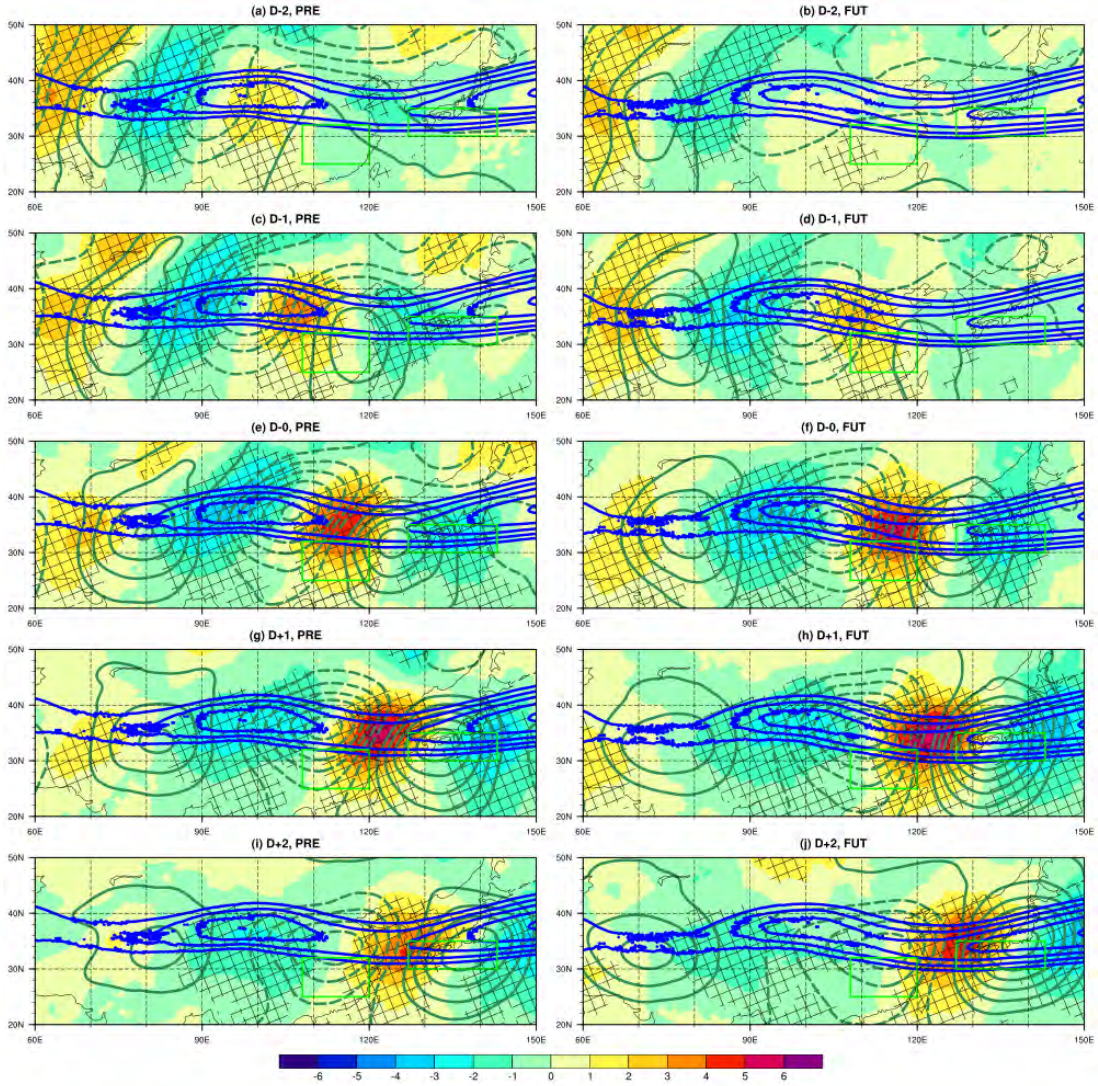

Fig. 5.4: Hovmöller diagram of composite map of v300' (shading; units: m s^{-1}) and Ψ300' (green contours; separated by every 2 × 10^6 m^2 s^{-1}) from day -2 (D-2) to day +2 (D+2) over Eastern China (25-32N, 108-120E). They are computed based on MRI-AGCM3.2S outputs from June to mid-July, for the (a, c, e, g, i) present climate and the (b, d, f, h, j) future climate respectively. Dashed (solid) green contours represent negative (positive) sign of Ψ300', and the zero-line of Ψ300' is not drawn in the panels. Blue contours (separated by every 2 m s^{-1}) represent the climatological mean zonal wind speed at 300 hPa (only ≥ 18 m s^{-1} is shown) from June to mid-July. Cross-hatches indicate that the v300' anomalies are statistically significant at the 90% confidence level or above according to the two-sided student's t test.

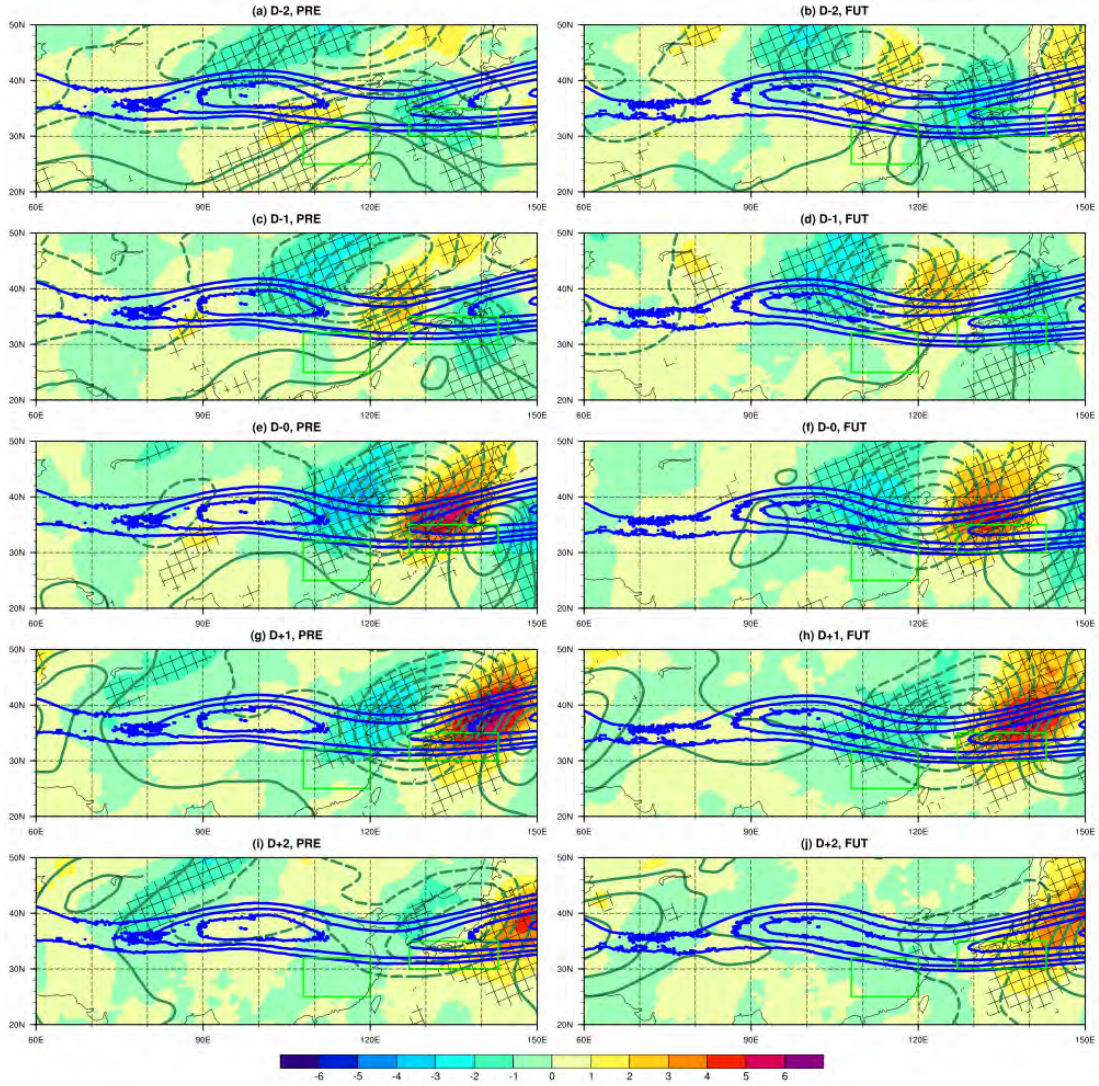

Fig. 5.5: As in Fig. 5.4, but for day -2 to day +2 over Baiu rainband (30-35N, 127-143E).

Hovmöller diagrams of the v300' composites, from day -2 to day +2, are also computed, so as to better visualize the eastward propagation of wave signals. From Fig.5.6, it can be clearly seen that the strongest positive $v300_{6hr}$' signal of the synoptic-scale wave trains passes through the search region (at day 0) with almost the same phase speed in the present as well as the future climate simulations. The propagating wave signals seem to slow down slightly at day +1 and day +2 in both regions, but such change is too small and may not be related to the phase speed at day 0. Since the background subtropical jet stream is projected to change slightly in its position and

intensity, we are going to examine whether the mean phase speed of the embedded transient wave signals is projected to change significantly. By tracking positions of the strongest positive mean wave signals from day -1 to day +1, a linear regression line joining those maximum signal positions at consecutive synoptic hours is drawn in the Fig. 5.6. The mean phase speed of the wave signals can then be estimated by the best-fitted slope. Based on two-sided Monte Carlo permutation tests, there is no significant change (at the 90% significance level) of the phase speed in these two regions.

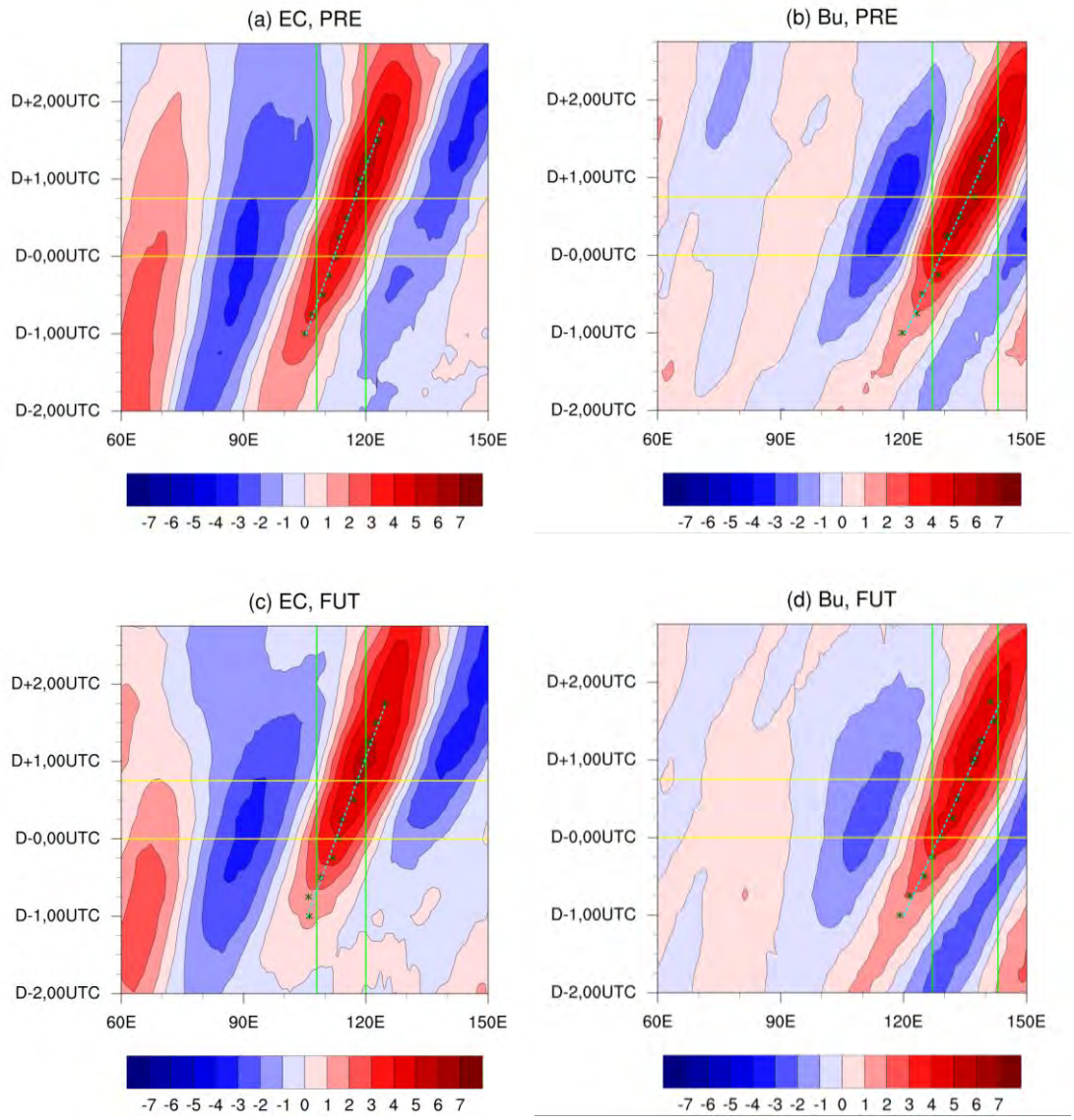

Fig. 5.6: Hovmöller diagram of $v300_{6hr}$' averaged over latitudinal band of (a, c) 30-40N for Eastern China (25-32N, 108-120E) and (b, d) 32-42N for Baiu rainband (30-35N, 127-143E) respectively, based on composites from day -2 (D-2) to day +2 (D+2). They are computed based on MRI-AGCM3.2S outputs for the (a, b) present climate and the (c, d) future climate respectively. Dark green stars denote the strongest positive v300' signals at every synoptic hour from day -1 (D-1) to day +1 (D+1). Cyan dash line indicates the linear regression line of these stars. Horizontal yellow lines indicate 00 UTC and 18 UTC for day 0, and vertical green lines indicate longitudinal boundaries of the respective region.

5.2.2. Three-dimensional circulation structure of waves

Since the upper-level disturbances are associated with low-level eddies, we also examine the projected change of the low-level relative vorticity (ζ850') and wind anomalies (wind850'). Fig. 5.7 shows the composite maps of them for day 0 in the present and future climate simulations respectively. From Figs. 5.7a and 5.7c, an elongated zone of positive ζ850' signal orientated along the southwest to the northeast direction is seen to influence the EC region in both present and future climate simulations. However, such positive ζ850' signal is obviously weakened in the globally warmed future. From Figs. 5.7b and 5.7d, anomalous cyclonic systems are found influencing the Bu region; again the associated positive ζ850' signal is weakened and is shifted westward near southern Japan in the future. Since the structure of the low-level circulation for EC and Bu regions is somehow different, here the area average of day 0 positive signals of ζ850' composite within 105 to 125E, 22 to 37N for the EC region, and 120 to 140E, 25 to 40N for Bu region, will be taken to estimate its projected change in amplitudes. The averaged ζ850' intensity is found to decrease by about 3 % for both regions, which is (not) significant at the 90% significance level based on one-sided Monte Carlo permutation tests for the EC (Bu) region.

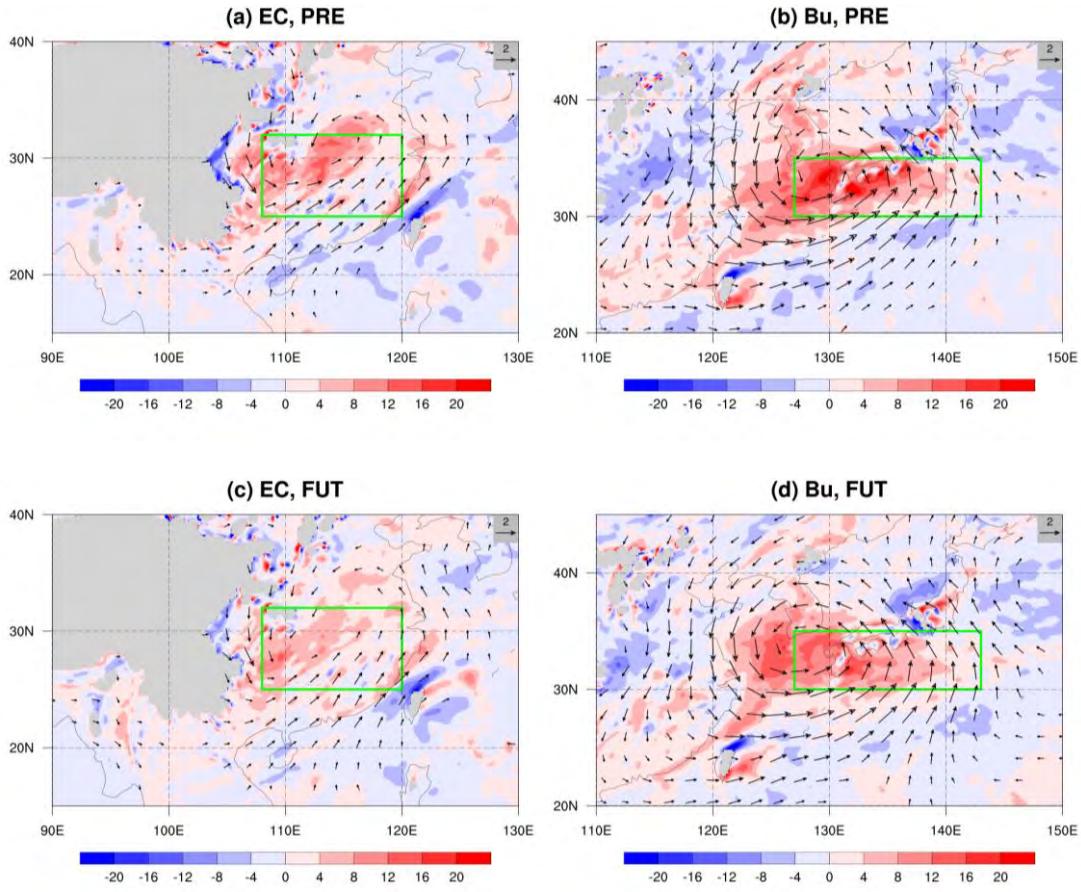

Fig. 5.7: Composite map of ζ850' (shading; units: 10^{-6} s^{-1}) and wind850' (see scale arrow at the top right; units: m s^{-1}) for day 0 over (a, c) Eastern China (25-32N, 108-120E) and (b, d) Baiu rainband (30-35N, 127-143E). They are computed based on MRI-AGCM3.2S outputs from June to mid-July, for the (a, b) present climate and the (c, d) future climate respectively. Arrows for wind850' are drawn only if either zonal or meridional component of the wind850' is statistically significant at the 90% confidence level or above according to the two-sided student's t test.

Anomalous low-level convergence (convg850') is another important variable since it is closely related to the precipitation characteristics associated with those disturbances. Fig. 5.8 shows the variation of convg850' composites from the present to the future climate. As shown in the composites, anomalous low-level divergence (convergence) can be found to the west (east) of both regions, but with generally reduced magnitude from the present to future climate. Stronger signals in the 850 hPa anomalous convergence are generally found within the EC or Bu regions, indicative

of its important role on determining the regional precipitation. The reduction of regionally averaged convg850' on day 0 due to global warming is 19 (6 %) for the EC (Bu) region, which passes (does not pass) the 90% significance level.

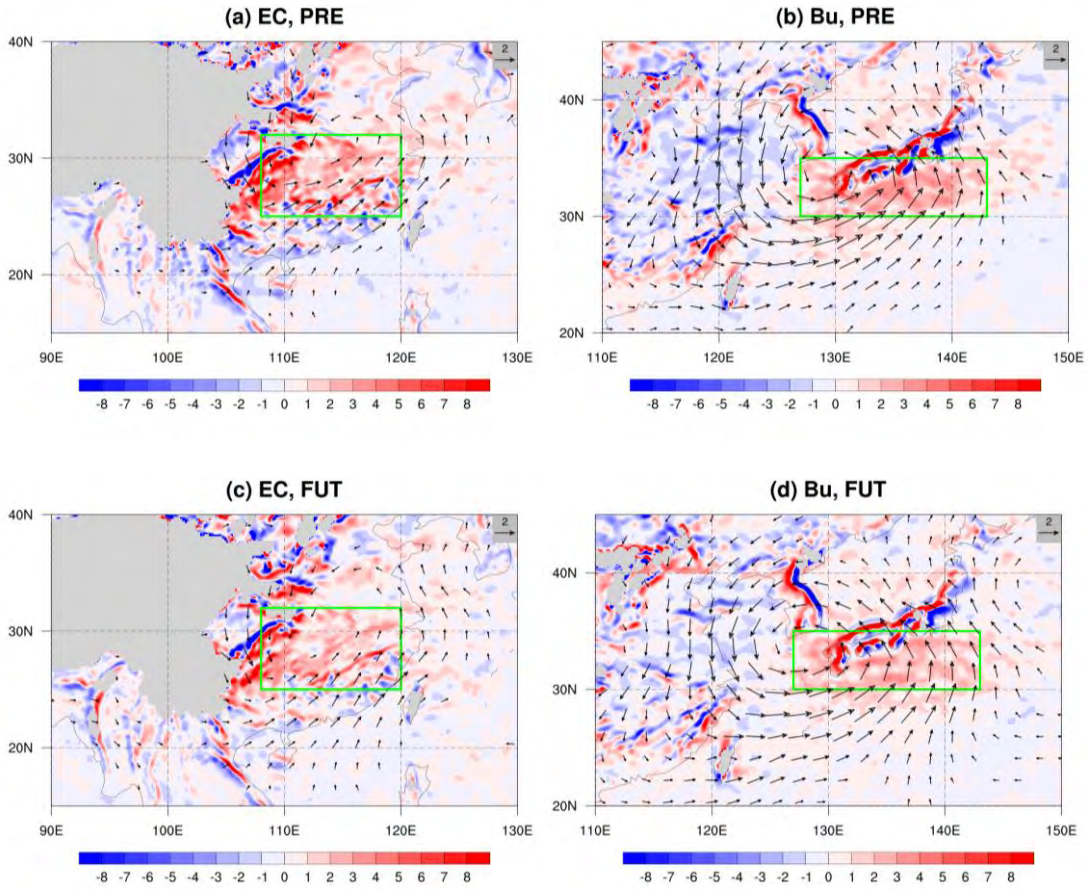

Fig. 5.8: As in Fig. 5.7, but for convg850' (shading; units: 10^{-6} s^{-1}).

As the southwest monsoon coming from the lower latitudes are often associated with heavy rainfall and low-level convergence, their projected changes are also examined. Composite maps of speed of 850 hPa wind are shown in Fig. 5.9, so as to reveal their projected changes due to global warming. Southwesterly wind (defined as daily mean wind with positive zonal and meridional components) within 105 to 120E, 22 to 32N for EC, 125 to 140E, 25 to 35N for Bu, is first identified. The

magnitude of its projection onto the northeastward direction is then calculated. It is found that the magnitude of those southwesterly wind component on day 0 is projected to increase (decrease) slightly for those influencing EC (Bu) region. However, by repeating the same calculations on the anomalous wind, the anomalous southwesterly wind component on day 0 weakens slightly for those affecting both regions in the globally warmed future.

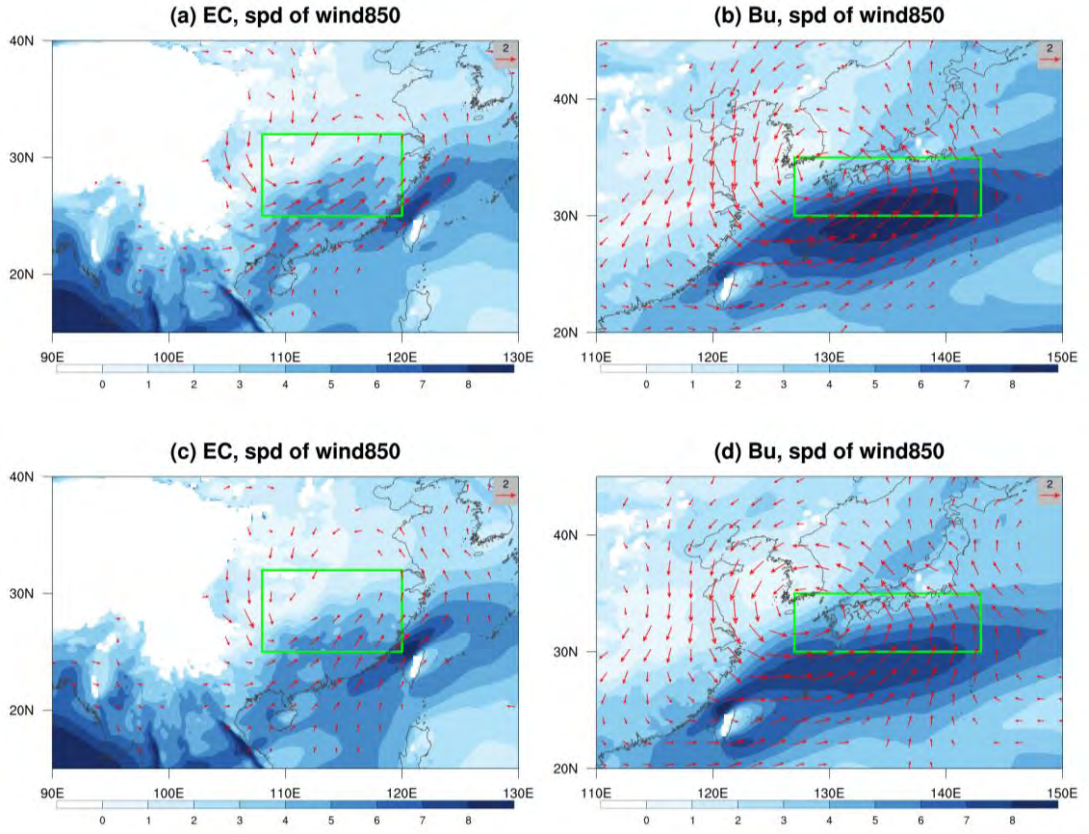

Fig. 5.9: As in Fig. 5.7, but for speed of wind850 (shading; units: m s^{-1}).

Besides the anomalous wind circulation, low-level temperature (t850') and wind anomalies (wind850'), as well as their placement, are important parameters when considering the baroclinic systems. Fig. 5.10 shows the composite maps of t850' and wind850' in both the present and future climate simulations. From the composites, cold and warm anomalies are found respectively to the northwest and southeast of the

EC or Bu regions. It can also be discerned that the warm anomalies for EC (Figs. 5.10a and 5.10c) and cold anomalies (Figs. 5.10b and 5.10d) for Bu, is weakened in the future climate projection. To quantify how such a change of circulation affects the low-level meridional heatflux, 5-day-mean low-level meridional heatflux ($\Phi_{q,5day}$) is calculated by taking 5-day average of product of composite v850' and t850' from day -2 to day +2. The changes of $\Phi_{q,5day}$ from the present to the future climate simulations are then shown in Fig. 5.11. From the figure, it can be seen that $\Phi_{q,5day}$ computed for waves affecting EC exhibits slight weakening over southeastern China, but is strongly reduced near northeastern China. The decrease of the meridional heatflux for waves affecting Bu is also found from the southeast to northeast China and over the East China Sea. Such findings are generally consistent with the weakening of those disturbances, since low-level meridional heatflux is associated with baroclinic interaction, which explains the growth of baroclinic system in the mid-latitudes.

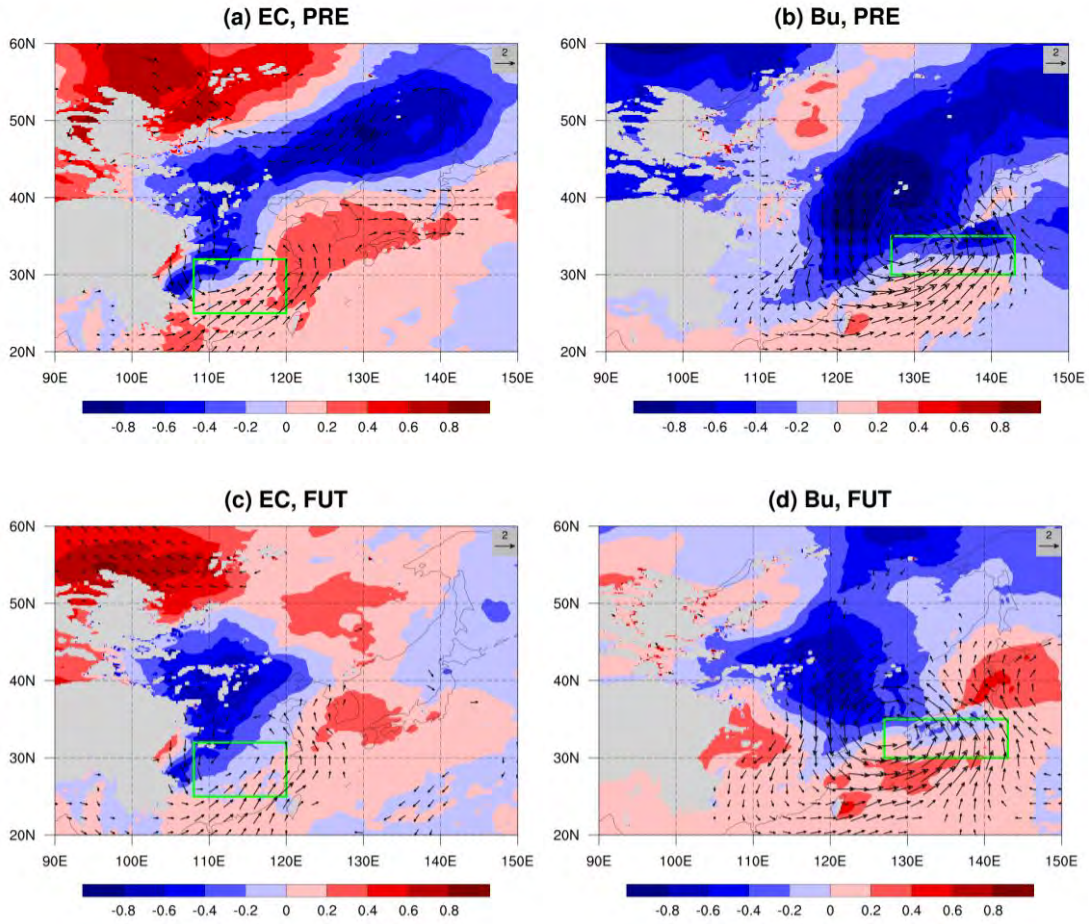

Fig. 5.10: As in Fig. 5.7, but for t850' (shading; units: K).

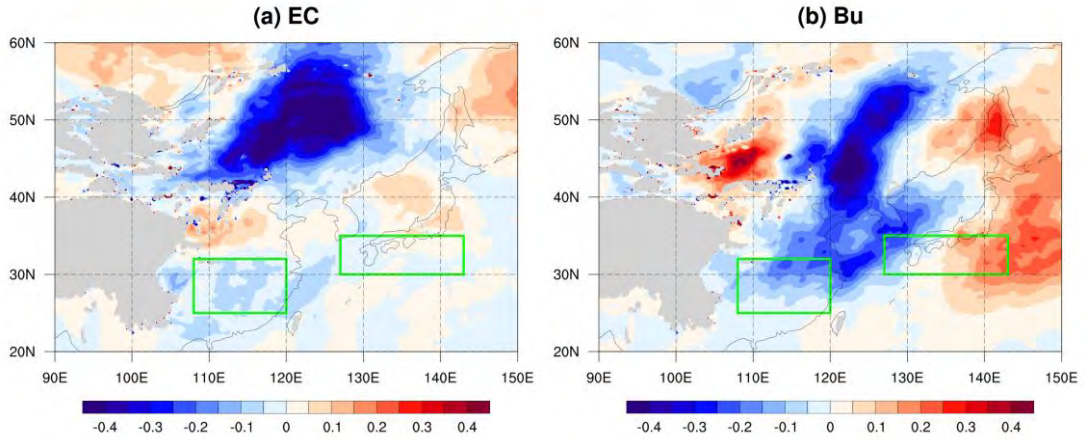

Fig. 5.11: Globally-warmed minus present-day $\Phi_{q,5day}$ (units: K m s^{-1}) for (a) Eastern China (25-32N, 108-120E) and (b) Baiu rainband (30-35N, 127-143E) based on MRI-AGCM3.2S outputs.

It is also worthwhile to examine how the anomalous vertical velocity (omg500') changes from the present to the future climate. The composite maps of omg500' in the present and future climate simulations are computed and shown in the Fig. 5.12. From the figure, the anomalous upward (downward) motion over the two regions (the upstream positions) becomes weaker under the warmed future. Such weakening is highly consistent with that found in the associated upper-level waves and low-level circulation. Here, regionally averaged negative omg500' is examined. Based on one-sided Monte Carlo permutation tests, the change of the averaged magnitude of the upward motion over both regions, however, does not pass the 90% significance level. On the other hand, the spatial coverage of the strong anomalous upward motion within both search regions is also found to further spread out in the future climate simulations. Also, there is no significant change of the anomalous 10m wind (wind10m') magnitude in the globally warmed future.

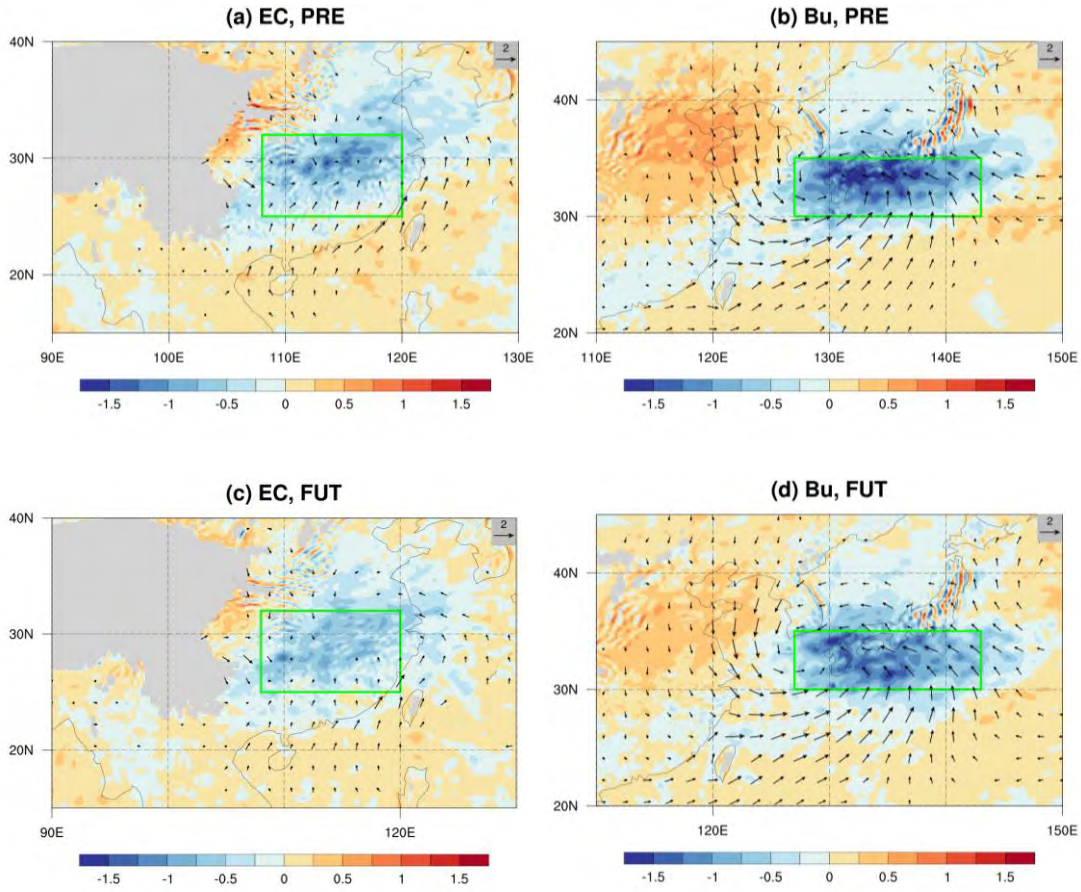

Fig. 5.12: As in Fig. 5.7, but for omg500' (shading; units: Pa s^{-1}) and wind10m' (arrows, units: m s^{-1}).

5.2.3. Anomalous precipitation and extremes

With significant decrease in the intensity of associated synoptic-scale systems influencing both EC and Bu regions, the projected change of the corresponding precipitation is now analyzed. Fig. 5.13 shows the composite maps of total precipitation (pp'), sea level pressure (slp') and 10m wind anomalies (wind10m'), based on the present and future climate simulations. It can be seen that under the future climate, negative sea level pressure anomalies become weaker for EC region; for Bu, weaker pressure gradients can also be discerned. On the other hand, the surface low influencing Bu tends to become broader in the globally warmed future. Although the

associated anomalous total precipitation (pp') is displaced slightly southward within the EC region, the regionally averaged pp' for EC (Bu) region increases by 0.2 (13) % from the present to the future climate. Although the associated synoptic-scale systems affecting both EC and Bu regions become weaker in the future climate, there still exist positive changes of those regionally averaged pp' due to global warming.

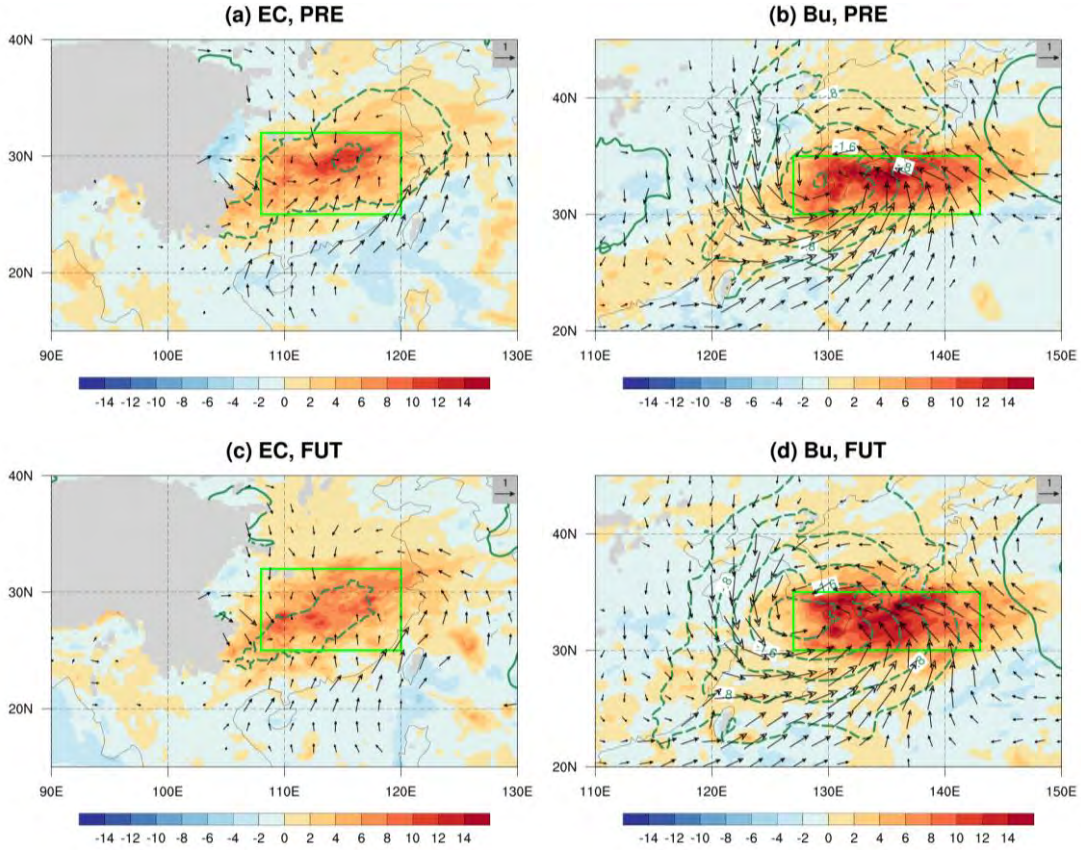

Fig. 5.13: Composite map of pp' (shading; units: mm day^{-1}), slp' (contour; units: hPa) and wind10m' (see scale arrow at top right; units: m s^{-1}) for day 0 over (a, c) Eastern China (25-32N, 108-120E) and (b, d) Baiu rainband (30-35N, 127-143E). They are computed based on MRI-AGCM3.2S outputs from June to mid-July, for the (a, b) present climate and the (c, d) future climate respectively. Arrows for wind10m' are drawn only if either zonal or meridional component of the wind10m' is statistically significant at the 90% confidence level or above according to the two-sided student's t test.

To further examine on the influence of wave-related extreme precipitation, the change of the contribution of extreme precipitation to the anomalous total precipitation (ext_{cont}) is also examined. An extreme precipitation event (extreme case) is defined whenever daily precipitation exceeds the R95p over wet days (refer to Chapter 3; from June to mid-July only). From Fig. 5.14, the patterns of ext_{cont} are almost the same as those of pp' in Fig. 5.13. Results show that more than 90% (80%) of regional average pp' over EC (Bu) region in the present climate is contributed by extreme precipitation, and both of these percentages are found to increase due to global warming. The regionally averaged ext_{cont} is projected to increase from 4.56 to 4.82 (6.84 to 7.93) mm day^{-1} for EC (Bu), indicating the intensification of both the anomalous total and extreme precipitation, regardless of the weakening of the associated synoptic-scale systems in the future climate projections.

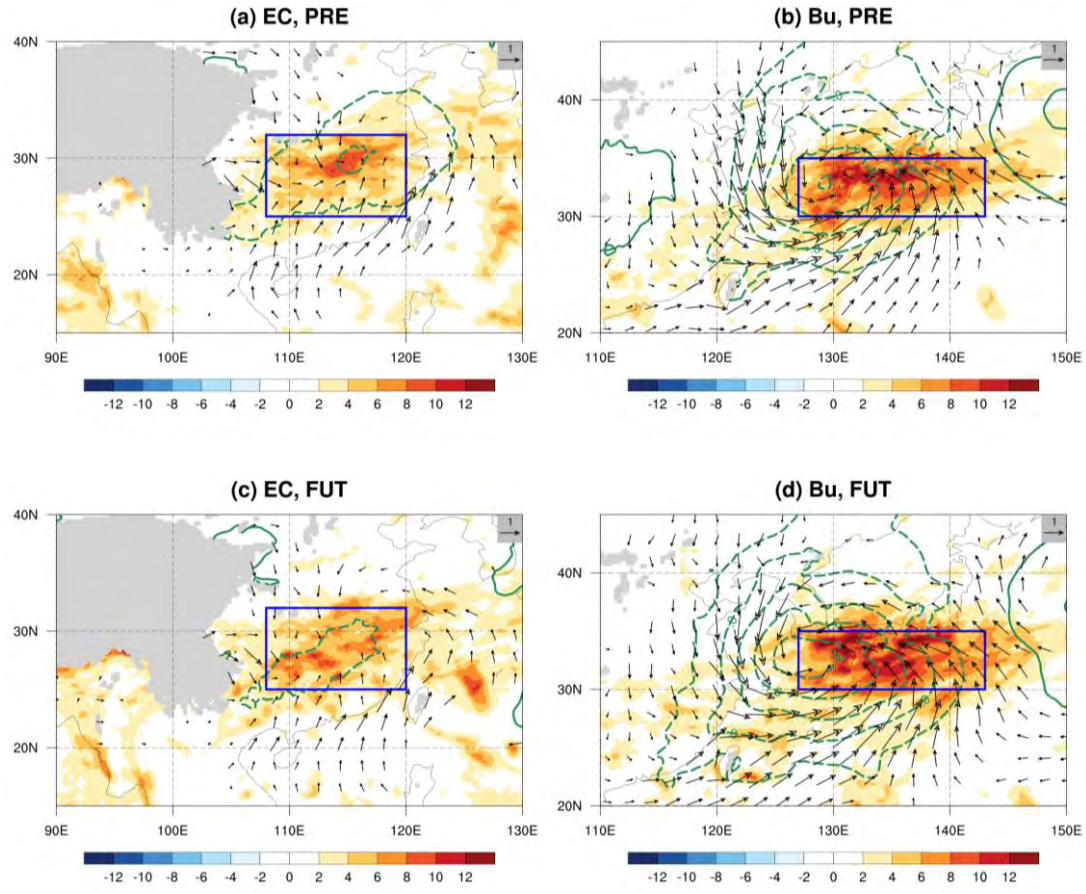

Fig. 5.14: As in Fig. 5.13, but for ext_{cont} *(shading; units: mm day*$^{-1}$*).*

Besides changes of extreme rainfall magnitudes, how the occurrence probability of extremes might be modulated is also studied. Fig. 5.15 shows the probability of occurrence of extreme cases (refer to Chapter 3; from June to mid-July only), computed by dividing the total count of extreme cases on day 0 by the total number of day 0, from the present to the future climate. From Fig. 5.15, it can be seen that the maximum occurrence probability of extreme cases is projected to decrease slightly within both regions in the future climate projection. Such patterns of reduction are generally consistent with those of the weakened anomalous vertical velocities as shown in Fig. 5.12. Since heavy precipitation is likely to occur within the ascending motion induced by those synoptic-scale systems, weakening of those systems may help explain the slightly less frequent extreme cases on day 0 in the future.

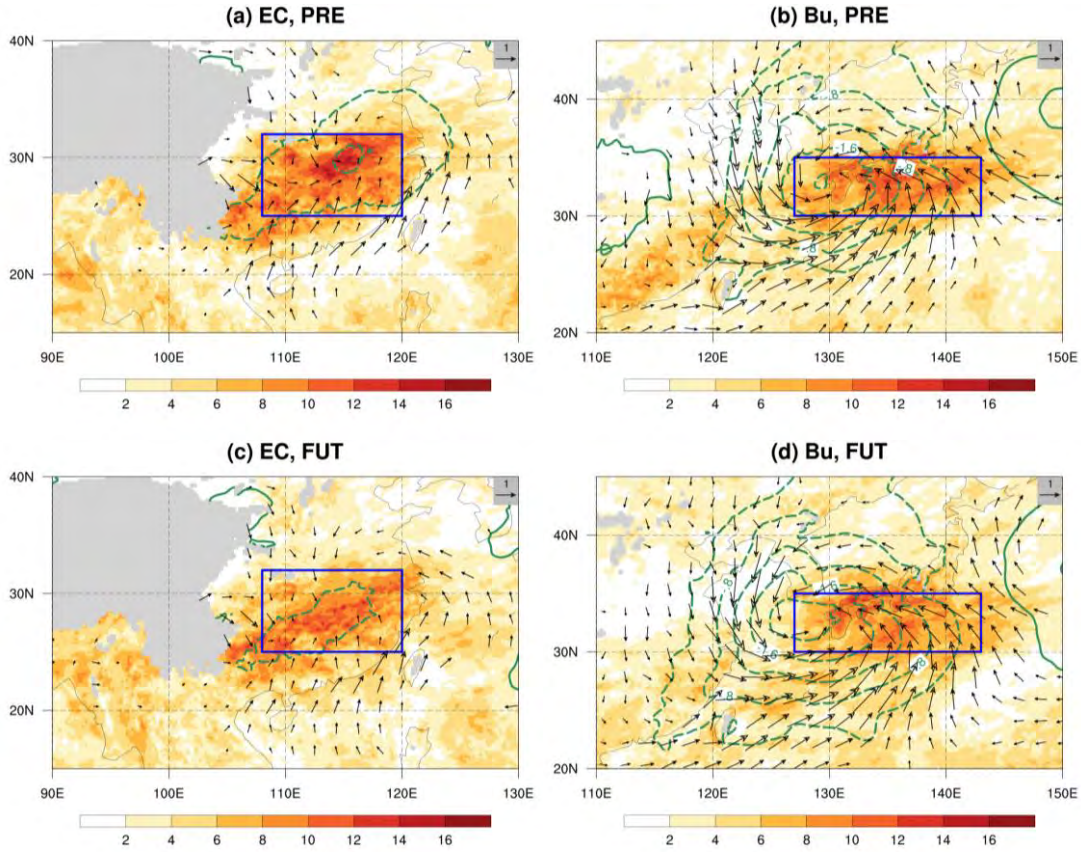

Fig. 5.15: As in Fig. 5.13, but for probability of occurrence of extreme cases (shading; units: %).

5.3. CC relation and change of basic state

Before investigating the relative roles of thermodynamic and dynamic effects in forming extreme precipitation, changes of basic state due to global warming is first examined. Fig. 5.16 shows the projected changes of different thermodynamic variables at various levels in the globally warmed future. It can be seen that the three-dimensional change of temperature distribution varies strongly from place to place over Asia and western north Pacific. Low-level warming is particularly strong from the northwest to eastern rim of the Tibetan Plateau (Fig. 5.16a). According to Liu et al. (2009), the projected warming is more prominent at higher elevations, and it is likely to be related to snow-albedo and complicated cloud-radiation feedbacks. Such warming reduces the low-level temperature gradient meridionally in central-east China (Fig. 5.16c), which might explain the stronger weakening of low-level circulation in EC region than that in Bu region. Instead, the upper-level warming is especially intense south of 30N and to a lesser extent north of 45N (Fig. 5.16b). Since the warming patterns at upper and low levels are quite different, layer-mean temperature (from the surface to 300 hPa) gradient is also examined. From Fig. 5.16d, such gradient is found to decrease in most of the mid-latitudes, with the exception of small increase near Mongolia and southern Japan. Such finding is consistent with the projected changes of subtropical jet stream, and it will be discussed later together with Fig. 5.17. The differential warming patterns also result in widespread increment of static stability (N) at 700 hPa over northern to northeastern Asia, southern Asia and over western North Pacific (Fig. 5.16e). It is also found that the main regions of reduced $\Phi_{q,5day}$ shown in Fig. 5.11 overlap with those in which there is increased static stability, near northeast Asia (Fig. 5.16e). This suggests that the enhanced low-level

stability might contribute to the weakening of the synoptic-scale waves in the mid-latitudes.

The change of baroclinity is also examined by calculating the Eady growth rate:

$$\sigma_E = 0.3098 \cdot \frac{|f| \left|\frac{\partial u}{\partial z}\right|}{N}$$

(Vallie, 2006; Simmonds and Lim, 2009), where f is the Coriolis parameter, u is the zonal wind speed and N is the Brunt-Väisälä frequency. σ_E is commonly used to reflect the baroclinity by combining the horizontal temperature gradient and the static stability. However, since it is unclear that which level would be the most informative for representing the baroclinity (e.g. Lim and Simmonds, 2007), changes of σ_E at both 700 hPa (based on data on the 500 and 850 hPa levels) and 500 hPa (based on data from 300 and 700 hPa levels) are both calculated. Similar pattern of projected changes is found at these levels, but the increase at 700 hPa in the vicinity of Mongolia becomes very weak at 500 hPa. Here, we will consider changes of σ_E at 500 hPa which is less noisy. From Fig. 5.16f, it can be seen that the seasonal mean σ_E is projected to decrease over most of the East Asian mid-latitudes, with the exception of a slight increase around the Mongolia probably due to heating effect over the Tibetan Plateau. Since the wave trains influencing both two regions (as shown in Figs. 5.4 and 5.5) generally propagate along the regions with negatively changed σ_E, such pattern of changes is highly consistent with the general weakening of baroclinic systems influencing both the EC and Bu regions.

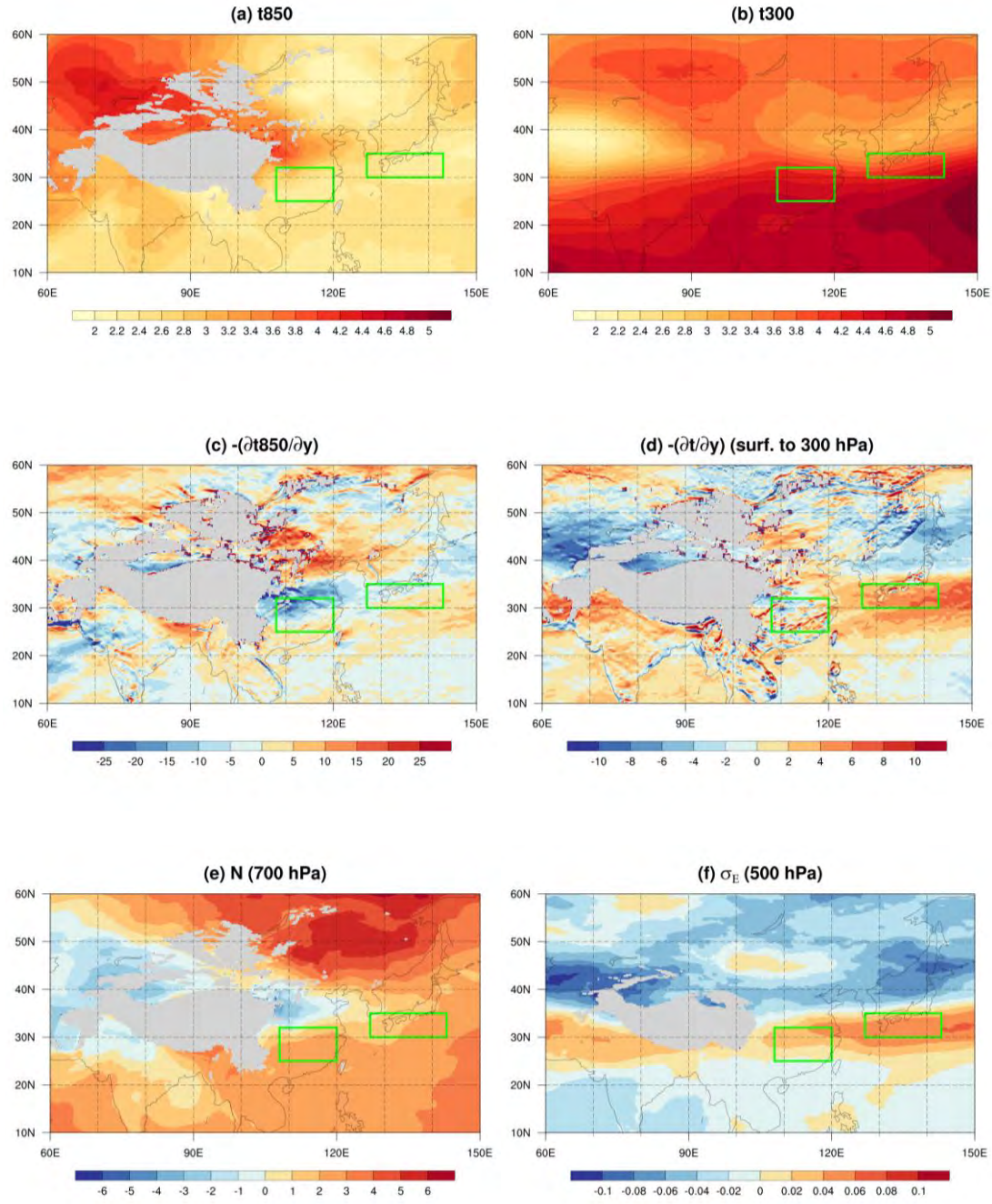

Fig. 5.16: Globally-warmed minus present-day value of temperature at (a) 850 hPa (units: K) and (b) 300 hPa (units: K), negative of meridional gradient of temperature (c) at 850 hPa (units: 10^{-7} K m^{-1}), and (d) averaged from surface to 300 hPa (units: 10^{-7} K m^{-1}) (e) Brunt-Väisälä frequency at 700 hPa (units: 10^{-4} s^{-1}) and (f) Eady Growth rate (units: day^{-1}) averaged for June-to-mid-July, based on MRI-AGCM3.2S outputs.

Besides the projected change of temperature distribution over Asia and western North Pacific, a general weakening of early-summer circulation over the mid-latitudes is also found in the globally warmed climate. Fig. 5.17 shows the projected changes of climatological mean wind at upper and low levels respectively, as well as those related to variance of v300', due to global warming. From Fig. 5.17a, the upper-level mean zonal wind is found to intensify (weaken) in the zonal band of (north of) 20-35N in the future. (Figs. 5.17a and 5.17b). From Fig. 5.17c, the weakening of mid-latitude early-summer circulation is accompanied by reduced variance of v300' in the projections. Such decrease of variance is particularly strong in most of the mid-latitudes, but relatively weak in the central and north of China. Those regions with significant reduction of variance generally coincide with those of upstream trough signals influencing both EC and Bu regions on day 0 (see Fig. 5.2), and thus are consistent with the significant weakening of the synoptic-scale waves influencing them. In general, the early-summer circulation over most places in the Asian mid-latitudes weakens in the globally warmed climate, and such weakening is probably related to the slightly southward shift of the subtropical jet stream. The changes of circulation in the low-latitudes, however, differ from those of the mid-latitudes. They include the weakening of low-level southwesterlies affecting the India, but intensification (or westward extension) of the subtropical high over the South China Sea and east of the Philippines.

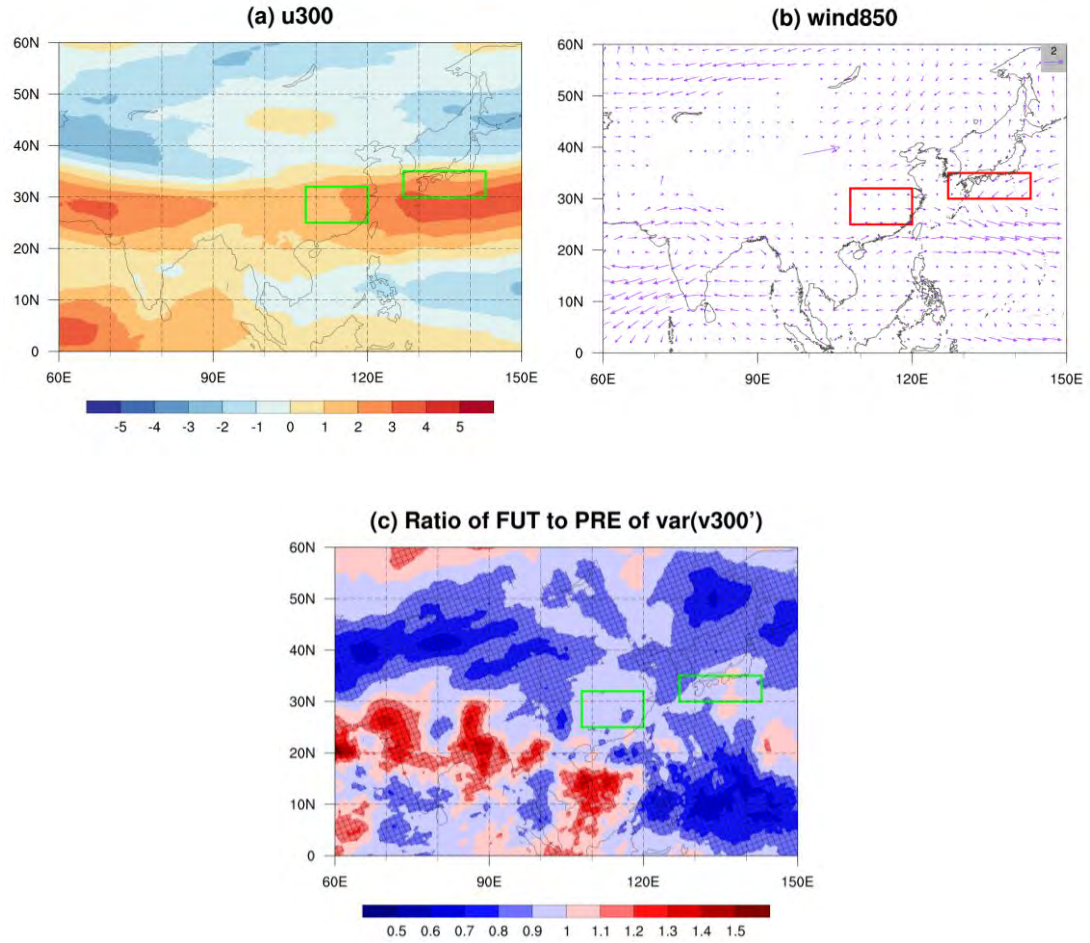

Fig. 5.17: Globally-warmed minus present-day value of mean (a) zonal wind at 300 hPa (units: m s^{-1}) and (b) wind at 850 hPa (see scale arrow at top right; units: m s^{-1}), and (c) ratio of globally-warmed to present-day value of variance of v300' from June to mid-July based on MRI-AGCM simulations. Cross-hatches in (c) indicate that the ratios of variance are statistically significant at the 90% confidence level or above according to the two-sided F-test.

After examination of the change of the background state, how global warming might affect the EC and Bu extreme rainfall associated with the synoptic-scale disturbance will be studied, in light of the CC-relation. In particular, the percentage change of the mean rainfall and various extreme precipitation indices per unit degree of lower-tropospheric warming, for each grid box, will be computed. The lower-tropospheric temperature is defined as the seasonal mean temperature (from June to mid-July) averaged between surface and 500 hPa level. Figs. 5.18 shows the

probability density function of percentage changes of those indices per unit degree warming within the EC and Bu regions. From Figs. 5.18a and 5.18b, it can be seen that changes of SDII, R95p and the average precipitation of extreme cases over both EC and Bu regions generally peak around 7 % K^{-1}, thus conforming to the CC relation. However, change of mean precipitation peak around 2 (6) % K^{-1} for EC (Bu) respectively. To further investigate the change of extreme rainfall associated with synoptic-scale systems, extreme rain days are further sampled to wave-related extreme days only. From Fig. 5.18c, the probability peaks for both mean rainfall and SDII are found to the left of those in Fig. 5.18a. In other words, the fractional change of wave-related rainfall per degree warming is less than that for all extreme events, and it is likely due to the significant weakening of systems in the EC region. On the other hand, for the Bu region, the mean rainfall and SDII statistics, computed for all days went right for wave-related days only, are very similar to each other (see Figs. 5.18b and 5.18d). Also, both distributions as well as R95p, are consistent with the CC-relation. The latter result highlights the importance of extremes in contributing to the mean precipitation in Bu, which is in marked contribution to rainfall in EC. In general, changes of R95p basically follow the CC-relation in both EC and Bu. For the EC region, mean rainfall and SDII do not follow CC-relation for wave-related days only, however, for the Bu region, all extreme indices and the mean rainfall seem to follow the CC-relation. The reason why the extreme indices still follow the CC-relation well is probably due to that the magnitude of weakening of the associated synoptic-scale systems is still too small to give a significant influence on the change of extreme precipitation.

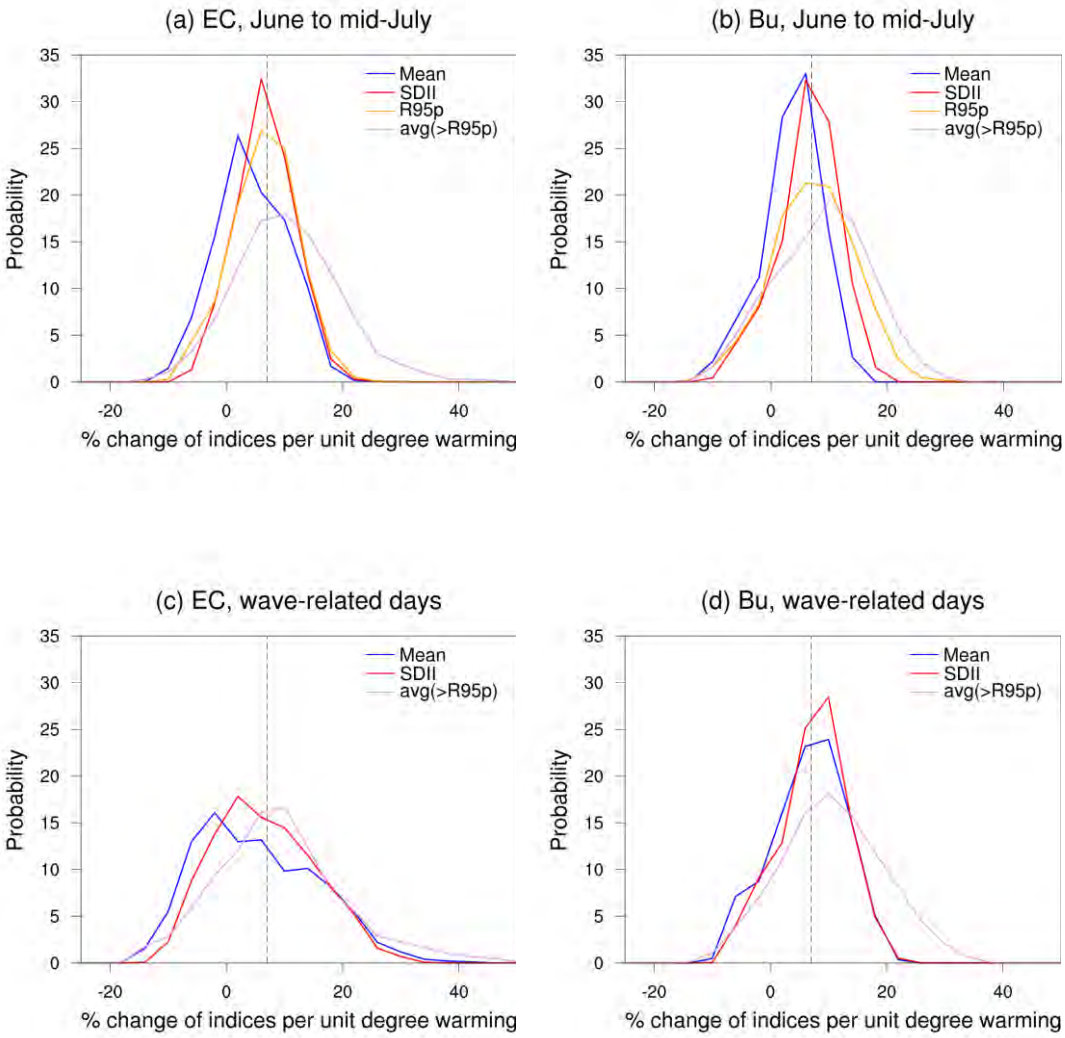

Fig. 5.18: Probability distribution (units: %) of percentage changes in the time mean precipitation rates (blue), SDII (red), R95p (orange), average precipitation of extreme cases (violet) per unit degree of warming in the lower-to-mid troposphere (a, b) from June to mid-July and (c, d) for wave-related extreme rainfall days only, in the globally-warmed compared to the present-day simulations over grid boxes within (a, c) Eastern China (25-32N, 108-120E) and (b, d) Baiu rainband (30-35N, 127-143E). The probability distribution of changes for R95p is shown only for upper panels. The vertical dashed line represents the change rate at 7 % K^{-1}, which is expected from the CC-relation. See text for details.

6. Limitations and Discussions

There are a number of potential limitations due to the use of the AGCM in the experiment. First of all, the AGCM is an atmospheric-only model, which completely neglects air-sea coupling. It may influence the simulated characteristics of TCs since their development draws lots of energy from the warm ocean surface but in turn cause large-scale mixing of near-surface sea water. Moreover, the model-simulated proportion of wet days within Meiyu-Baiu season is found to be greater than that of TRMM (figure not shown), which may result in some biases when simulating and projecting the precipitation characteristics. Also, the model tends to underestimate the early-summer southwesterly airstream and overestimate the springtime precipitation over the southeastern China, which may cause difficulties in understanding the projected change of precipitation characteristics. Those deviations are probably related to the modified cumulus parameterization scheme in the MRI-AGCM3.2S (compared with its previous version). Both the conversion rate (of cloud water to precipitation) and entrainment in the scheme were adjusted, which may impose unpredictable effects on the model-simulated precipitation. Besides, the spatiotemporal variability of precipitation as well as the internal variability of climate system may also influence the characteristics of model-simulated precipitation. On the other hand, although such a very high-resolution AGCM brought a lot of advantages in climate studies, it greatly increases the computational cost of any possible ensemble simulations. Whether 20-km resolution is good enough to capture characteristics of precipitation in different scales is also needed for further investigation. Indeed, uncertainties may also come from the projection of future climate. Since only the multi-model ensemble mean of projected changes of SST pattern was used as the lower boundary condition during simulation, it will lower the generality of the simulation outputs since the future

climate will be affected by the model bias of the AGCM. Furthermore, possible changes of anthropogenic forcing due to aerosols, urbanizations and land use changes hadn't been considered comprehensively, which may lead to difficulties in studying changes due to global warming only.

Besides, different interpretation of the simulation datasets may also influence the resulting projected changes. In order to examine whether defining anomalies by bandpass filtering instead may generate different results, the whole analysis was repeated with all the anomalies defined by 2.5-to-6-day bandpass filtering, and the results were compared to the original results with anomalies defined by just removal of seasonal mean. By using bandpass filtering, upper-level synoptic-scale waves are still projected to be weakened in the globally warmed climate. The only effect brought by the bandpass filtering is that, when compared to the original results, the magnitude of different variables decreases by nearly half, and the phase speed of wave signal is slightly higher. All those findings suggest that the analysis based on original definition of anomalies can yield reasonable characteristics for the synoptic-scale weather systems. Moreover, some may argue that whether the projected changes of the systems are sensitive to the third criterion, which is used to check the eastward propagation of wave signal in the wave-selection algorithm. Although the absence of such criterion is found not to greatly affect the final results, such criterion is necessary to guarantee that all the associated upper-level wave disturbances are propagating eastward and in the synoptic scale. On the other hand, the novel wave-selection algorithm was applied within the two regions only, which may also limit possible change of position of storm tracks. However, as shown in Figs. 5.4 and 5.5, the shift of position of subtropical jet stream and thus storm track is very small, and the pattern of precipitation composites over two regions only shifts southward slightly in the future climate. Moreover, the

association between extreme cases and upper-level synoptic-scale wave was studied mainly based on day 0. More informative signals should be discovered if different time lag from the day 0 can be analyzed in more details. Last but not least, the complex topography brought a lot of difficulties in explaining future changes of the systems influencing EC and Bu region. More aspects of projected variation of the background circulation should be examined in order to better understand the mechanism of projected weakening of the synoptic-scale systems over the study region.

7. Conclusions

In this study, we examined the projected change of Meiyu-Baiu extreme precipitation and the associated mid-latitude synoptic-scale weather systems over the EC and Bu regions, based on simulations from the 20-km MRI-AGCM3.2S. The model was first evaluated against the TRMM and the APHRODITE datasets, and it was demonstrated to give realistic temporal evolution and spatial distribution of Asian summer monsoon rainfall. In particular, the northward shifts of extreme rainfall activities associated with the Meiyu-Baiu rainband are well captured by the model simulations, but with the exception that there exists overestimation of the occurrence probability during spring for EC region.

From June to mid-July, it is found that there exists certain statistical relation between the upper-level wave signals and the regional precipitation based on the present climate simulation. After removal of all extreme cases related to tropical cyclones, a novel wave-selection algorithm was then developed on the basis of upper-level wave characteristics inspected from time composites. Three upper-level criteria within a rectangular selection domain in the northwest of each non-TC related extreme case location are used to identify the existence of upper-level propagating wave (trough) signals. The results are generally insensitive to the threshold values of three criteria used in the algorithm, and are found to give realistic outputs of the synoptic-scale systems in the East Asian mid-latitudes when compared to the observations/reanalysis dataset. The same algorithm, followed by the time clustering technique, was applied for both the present and future climate simulations, so as to infer the impacts of global warming on the behavior of these systems.

Results show that there is robust decrease of intensity of the systems influencing both EC and Bu region in the future climate. The associated upper-level

waves are projected to decrease significantly in mean amplitude by about 6%, without any significant change of mean phase speed. The corresponding low-to-mid circulation, including anomalous low-level convergence, relative vorticity and sea level pressure composites, is also projected to be weakened over both EC and Bu in the future climate. Such weakening of baroclinic weather systems is highly consistent with the pattern of projected decrease of Eady growth rate, and thus attributable to the background circulation changes in the projected future. Those changes are likely related to the widespread increment of static stability over the East Asian mid-latitudes, and also the greater reduction of low-level meridional temperature gradient over EC region. General slowing down of the mid-latitude background circulation is also found in the future climate simulation, which is probably related to the projected slightly southward shift of the subtropical jet stream.

However, the total and extreme precipitation within the Meiyu-Baiu season generally intensify over East Asia in the globally warmed future. The wave-associated anomalous precipitation over Bu are projected to intensify (but to a lesser extent for EC). Such intensification is mainly due to enhancement in the portion contributed from extreme rainfall, which are in marked contribution to the mean precipitation within both the EC and Bu region. The extreme rainfall increases as the background temperature in these regions warms, largely following the Clausius-Clapeyron relation. Therefore, changes of wave-related extreme precipitation in EC and Bu are mainly due to the thermodynamic effect, which seems to be much stronger than the dynamic effect due to the slight weakening of those weather systems.

8. Bibliography

Alexander, L.V., Zhang, X., Peterson, T. C., Caesar, J., Gleason, B., Klein Tank, A. M. G., … Vazquez-Aguirre, J. L. (2006). Global observed changes in daily climate extremes of temperature and precipitation. Journal of Geophysical Research Atmospheres, 111, 1–22. https://doi.org/10.1029/2005JD006290

Allen, M. R., and Ingram, W. J. (2002). Constraints on future changes in climate and the hydrologic cycle. Nature, 419(6903). https://doi.org/10.1038/nature01092

Barbero, R., Abatzoglou, J. T., and Fowler, H. J. (2018). Contribution of large-scale midlatitude disturbances to hourly precipitation extremes in the United States. Climate Dynamics, 1–12. https://doi.org/10.1007/s00382-018-4123-5

Berbery, E. H., & Vera, C. S. (1996). Characteristics of the Southern Hemisphere Winter Storm Track with Filtered and Unfiltered Data. *Journal of the Atmospheric Sciences*, *53*(3), 468–481.

Catto, J. L., Madonna, E., Joos, H., Rudeva, I., and Simmonds, I. (2015). Global Relationship between Fronts and Warm Conveyor Belts and the Impact on Extreme Precipitation. Journal of Climate, 28(21), 8411–8429. https://doi.org/10.1175/JCLI-D-15-0171.1

Chang, E. K. M. (1993). Downstream Development of Baroclinic Waves As Inferred from Regression Analysis. *Journal of the Atmospheric Sciences*, *50*(13), 2038–2053.

Chang, E. K. M., & Yu, D. B. (1999). Characteristics of Wave Packets in the Upper Troposphere. Part I : Northern Hemisphere Winter. *Journal of the Atmospheric Sciences*, *56(11)*, 1708–1728.

Chen, S., Hong, Y., Cao, Q., Gourley, J. J., Kirstetter, P.-E., Yong, B., … Hardy, J. (2013). Similarity and difference of the two successive V6 and V7 TRMM multisatellite precipitation analysis performance over China. Journal of Geophysical Research: Atmospheres, 118(23), 13,060-13,074. https://doi.org/10.1002/2013jd019964

Chen, T. J. G., and Chang, C. P. (1980). The Structure and Vorticity Budget of an Early Summer Monsoon Trough (Mei-Yu) over Southeastern China and Japan. Monthly Weather Review, 108, 942–953.

Coumou, D., Lehmann, J., and Beckmann, J. (2015). The weakening summer circulation in the Northern Hemisphere mid-latitudes. Science, 348(6232), 324–327. https://doi.org/10.1126/science.1261768

Davies, H. C. (2015). Weather chains during the 2013/2014 winter and their significance for seasonal prediction. Nature Geoscience, 8(11), 833–837. https://doi.org/10.1038/ngeo2561

Dee, D. P., Uppala, S. M., Simmons, A. J., Berrisford, P., Poli, P., Kobayashi, S., … Vitart, F. (2011). The ERA-Interim reanalysis: configuration and performance of the data assimilation system. Quarterly Journal of the Royal Meteorological Society, 137(656), 553–597. https://doi.org/10.1002/qj.828

Ding, Y. (1992). Summer Monsoon Rainfalls in China. Journal of the Meteorological Society of Japan, 70(1B), 373–396.

Ding, Y., and Chan, J. C. L. (2005). The East Asian summer monsoon : an overview. Meteorology and Atmospheric Physics, 89(1), 117–142. https://doi.org/10.1007/s00703-005-0125-z

Ding, Y., Liu, J., Sun, Y., Liu, Y., He, J., and Song, Y. (2007). A Study of the Synoptic-Climatology of the Meiyu System in East Asia. Chinese Journal of Atmospheric Sciences, 31(6), 1082–1101. (in Chinese).

Ding, Y., and Sikka, D. R. (2006). Synoptic systems and weather. In B. Wang (Ed.), The Asian Monsoon (pp. 131–201). https://doi.org/10.1007/3-540-37722-0_4

Donat, M. G., Alexander, L.V., Yang, H., Durre, I., Vose, R., Dunn, R. J. H., … Kitching, S. (2013). Updated analyses of temperature and precipitation extreme indices since the beginning of the twentieth century: The HadEX2 dataset. Journal of Geophysical Research: Atmospheres, 118(5), 2098–2118. https://doi.org/10.1002/jgrd.50150

Donat, M. G., Lowry, A. L., Alexander, L.V., O'Gorman, P. A., and Maher, N. (2016). More extreme precipitation in the world's dry and wet regions. Nature Climate Change, 6(5), 508. https://doi.org/10.1038/nclimate2941

Eady, E. T. (1949). Long Waves and Cyclone Waves. Tellus, 1(3), 33–52. https://doi.org/10.3402/tellusa.v1i3.8507

Emori, S., and Brown, S. J. (2005). Dynamic and thermodynamic changes in mean and extreme precipitation under changed climate. Geophysical Research Letters, 32(17), 1–5. https://doi.org/10.1029/2005GL023272

Fang, J., Yang, W., Luan, Y., Du, J., Lin, A., and Zhao, L. (2019). Evaluation of the TRMM 3B42 and GPM IMERG products for extreme precipitation analysis over China. Atmospheric Research, 223, 24–38. https://doi.org/10.1016/J.ATMOSRES.2019.03.001

Fink, A. H., Brücher, T., Ermert, V., Krüger, A., and Pinto, J. G. (2009). The European storm Kyrill in January 2007: Synoptic evolution, meteorological impacts and some considerations with respect to climate change. Natural Hazards and Earth System Science, 9(2), 405–423. https://doi.org/10.5194/nhess-9-405-2009

Francis, J. A., and Vavrus, S. J. (2012). Evidence linking Arctic amplification to extreme weather in midlatitudes. Geophysical Research Letters, 39(6). https://doi.org/10.1002/grl.50880

Geng, Q., and Sugi, M. (2002). Possible Change of Extratropical Cyclone Activity due to Enhanced Greenhouse Gases and Sulfate Aerosols - Study with a High-Resolution AGCM. Journal of Climate, 16(13), 2262–2274. https://doi.org/10.1175/1520-0442(2003)16<2262:PCOECA>2.0.CO;2

Hawcroft, M. K., Shaffrey, L. C., Hodges, K. I., and Dacre, H. F. (2012). How much Northern Hemisphere precipitation is associated with extratropical cyclones? Geophysical Research Letters, 39(24), 1–6. https://doi.org/10.1029/2012GL053866

Hewson, T. D., and Neu, U. (2015). Cyclones, windstorms and the IMILAST project. Tellus A: Dynamic Meteorology and Oceanography, 67(1). https://doi.org/10.3402/tellusa.v67.27128

Hoskins, B. J., McIntyre, M. E., and Robertson, A. W. (1985). On the use and significance of isentropic potential vorticity maps. Quarterly Journal of the Royal Meteorological Society, 111(470), 877–946. https://doi.org/10.1002/qj.49711147002

Hoskins, B. J., and Valdes, P. J. (1990). On the existence of Storm-Tracks. Journal of the Atmospheric Sciences, 47(15), 1854–1864.

Huffman, G. J., Adler, R. F., Bolvin, D. T., Gu, G., Nelkin, E. J., Bowman, K. P., … Wolff, D. B. (2007). The TRMM Multisatellite Precipitation Analysis (TMPA): Quasi-Global, Multiyear, Combined-Sensor Precipitation Estimates at Fine Scales. Journal of Hydrometeorology, 8(1), 38–55. https://doi.org/10.1175/jhm560.1

Japan Meteorological Agency (2007). Outline of the operational numerical weather prediction at the Japan Meteorological Agency (Appendix to WMO numerical weather prediction progress report).

Jiang, H., & Zipser, E. J. (2010). Contribution of Tropical Cyclones to the Global Precipitation from Eight Seasons of TRMM Data: Regional, Seasonal, and Interannual Variations. *Journal of Climate*, *23*(6), 1526–1543. https://doi.org/10.1175/2009jcli3303.1

Kitoh, A., Ose, T., Kurihara, K., Kusunoki, S., Sugi, M., and Kakushin Team-3 Modeling Group. (2009). Projection of changes in future weather extremes using super-high-resolution global and regional atmospheric models in the KAKUSHIN Program: Results of preliminary experiments. Hydrological Research Letters, 3, 49–53. https://doi.org/10.3178/hrl.3.49

Lehmann, J., and Coumou, D. (2015). The influence of mid-latitude storm tracks on hot, cold, dry and wet extremes. Scientific Reports, 5, 1–9. https://doi.org/10.1038/srep17491

Lenderink, G., and van Meijgaard, E. (2008). Increase in hourly precipitation extremes beyond expectations from temperature changes. Nature Geoscience, 1(8), 511–514. https://doi.org/10.1038/ngeo262

Lim, E. P., & Simmonds, I. (2007). Southern Hemisphere Winter Extratropical Cyclone Characteristics and Vertical Organization Observed with the ERA-40 Data in 1979-2001. *Journal of Climate*, *20*(11), 2675–2690. https://doi.org/10.1175/JCLI4135.1

Liu, X., Cheng, Z., Yan, L., & Yin, Z. Y. (2009). Elevation dependency of recent and future minimum surface air temperature trends in the Tibetan Plateau and its surroundings. *Global and Planetary Change*, *68*(3), 164–174. https://doi.org/10.1016/j.gloplacha.2009.03.017

Lui, Y. S., Tam, C. Y., and Lau, N. C. (2018). Future changes in Asian summer monsoon precipitation extremes as inferred from 20-km AGCM simulations. Climate Dynamics, 1–17. https://doi.org/10.1007/s00382-018-4206-3

Mesquita, M. D. S., Kvamstø, N. G., Sorteberg, A., and Atkinson, D. E. (2008). Climatological properties of summertime extra-tropical storm tracks in the Northern Hemisphere. Tellus, 60A, 557–569. https://doi.org/10.1111/j.1600-0870.2008.00305.x

Mizuta, R., Matsueda, M., Endo, H., and Yukimoto, S. (2011). Future Change in Extratropical Cyclones Associated with Change in the Upper Troposphere. Journal of Climate, 24(24), 6456–6470. https://doi.org/10.1175/2011JCLI3969.1

Mizuta, R., Oouchi, K., Yoshimura, H., Noda, A., Katayama, K., Yukimoto, S., … Nakagawa, M. (2006). 20-km-Mesh Global Climate Simulations Using JMA-GSM Model —Mean Climate States—. Journal of the Meteorological Society of Japan. Ser. II, 84(1), 165–185. https://doi.org/10.2151/jmsj.84.165

Mizuta, R., Yoshimura, H., Murakami, H., Matsueda, M., Endo, H., Ose, T., … Kitoh, A. (2012). Climate Simulations Using MRI-AGCM3.2 with 20-km Grid. Journal of the Meteorological Society of Japan. Ser. II, 90, 233–258. https://doi.org/10.2151/jmsj.2012-a12

Murakami, H., Wang, Y., Yoshimura, H., Mizuta, R., Sugi, M., Shindo, E., … Kitoh, A. (2012). Future Changes in Tropical Cyclone Activity Projected by the New High-Resolution MRI-AGCM. Journal of Climate, 25(9), 3237–3260. https://doi.org/10.1175/JCLI-D-11-00415.1

Ninomiya, K., and Akiyama, T. (1992). Multi-scale Features of Baiu, the Summer Monsoon over Japan and the East Asia. Journal of the Meteorological Society of Japan, 70(1B), 467–495. https://doi.org/10.2151/jmsj1965.70.1b_467

Ninomiya, K., and Shibagaki, Y. (2007). Multi-Scale Features of the Meiyu-Baiu Front and Associated Precipitation Systems. Journal of the Meteorological Society of Japan, 85B, 103–122. https://doi.org/10.2151/jmsj.85b.103

Pall, P., Allen, M. R., and Stone, D. A. (2007). Testing the Clausius-Clapeyron constraint on changes in extreme precipitation under CO2 warming. Climate Dynamics, 28(4), 351–363. https://doi.org/10.1007/s00382-006-0180-2

Pfahl, S., Madonna, E., Boettcher, M., Joos, H., and Wernli, H. (2014). Warm Conveyor Belts in the ERA-Interim Dataset (1979-2010). Part II: Moisture Origin and Relevance for Precipitation. Journal of Climate, 27(1), 27–40. https://doi.org/10.1175/JCLI-D-13-00223.1

Raveh-Rubin, S., and Wernli, H. (2015). Large-scale wind and precipitation extremes in the Mediterranean: A climatological analysis for 1979-2012. Quarterly Journal of the Royal Meteorological Society, 141(691), 2404–2417. https://doi.org/10.1002/qj.2531

Rayner, N. A., Parker, D. E., Horton, E. B., Folland, C. K., Alexander, L. V., Rowell, D. P., … Kaplan, A. (2003). Global analyses of sea surface temperature, sea ice, and night marine air temperature since the late nineteenth century. Journal of Geophysical Research, 108(D14). https://doi.org/10.1029/2002jd002670

Ren, X., Yang, X., and Chu, C. (2010). Seasonal variations of the synoptic-scale transient eddy activity and polar front jet over East Asia. Journal of Climate, 23(12), 3222–3233. https://doi.org/10.1175/2009JCLI3225.1

Rivière, G., Arbogast, P., and Joly, A. (2015). Eddy kinetic energy redistribution within windstorms Klaus and Friedhelm. Quarterly Journal of the Royal Meteorological Society, 141(688), 925–938. https://doi.org/10.1002/qj.2412

Romero, R., Martín, A., Homar, V., Alonso, S., and Ramis, C. (2006). Predictability of prototype flash flood events in the Western Mediterranean under uncertainties of the precursor upper-level disturbance. Advances in Geosciences, 7, 55–63. https://doi.org/10.5194/nhess-5-505-2005

Röthlisberger, M., Pfahl, S., and Martius, O. (2016). Regional-scale jet waviness modulates the occurrence of midlatitude weather extremes. Geophysical Research Letters, 43(20), 10,989-10,997. https://doi.org/10.1002/2016GL070944

Sampe, T., and Xie, S.-P. (2010). Large-Scale Dynamics of the Meiyu-Baiu Rainband: Environmental Forcing by the Westerly Jet. *Journal of Climate*, *23*(1), 113–134. https://doi.org/10.1175/2009JCLI3128.1

Sillmann, J., Kharin, V. V., Zwiers, F. W., Zhang, X., and Bronaugh, D. (2013). Climate extremes indices in the CMIP5 multimodel ensemble: Part 2. Future climate projections. Journal of Geophysical Research Atmospheres, 118(6), 2473–2493. https://doi.org/10.1002/jgrd.50188

Simmonds, I., & Lim, E. P. (2009). Biases in the calculation of Southern Hemisphere mean baroclinic eddy growth rate. *Geophysical Research Letters*, *36*(1), 1–5. https://doi.org/10.1029/2008GL036320

Solomon, S., Qin, D., Manning, M., Averyt, K., and Marquis, M. (2007). Climate change 2007-the physical science basis: Working group I contribution to the fourth assessment report of the IPCC. Cambridge University Press.

Tiedtke, M. (1993). Representation of Clouds in Large-Scale Models. Monthly Weather Review, 121, 3040–3061.

Trenberth, K. E. (1991). Storm Tracks in the Southern Hemisphere. *Journal of the Atmospheric Sciences*, *48*(19), 2159–2178.

Ulbrich, U., Leckebusch, G. C., and Pinto, J. G. (2009). Extra-tropical cyclones in the present and future climate: a review. Theoretical and Applied Climatology, 96(1–2), 117–131. https://doi.org/10.1007/s00704-008-0083-8

Utsumi, N., Kim, H., Kanae, S., and Oki, T. (2016). Which weather systems are projected to cause future change in mean and extreme precipitation in CMIP5 simulations? Journal of Geophysical Research: Atmospheres, 121, 10522–10537. https://doi.org/10.1002/2016JD025137.Received

Utsumi, N., Kim, H., Kanae, S., and Oki, T. (2017). Relative contributions of weather systems to mean and extreme global precipitation. Journal of Geophysical Research, 122(1), 152–167. https://doi.org/10.1002/2016JD025222

Vallis, G.K. (2006). Atmospheric and Oceanic Dynamics: Fundamentals and Large-Scale Circulation. Cambridge University Press.

Walland, D., and Simmonds, I. (1999). Baroclinicity, Meridional Temperature Gradients, and the Southern Semiannual Oscillation. Journal of Climate, 12(12), 3376–3382. https://doi.org/10.1175/1520-0442(1999)012<3376:BMTGAT>2.0.CO;2

Wang, B., and Lin, H. (2002). Rainy season of the Asian-Pacific summer monsoon. Journal of Climate, 15(4), 386–398. https://doi.org/10.1175/1520-0442(2002)015<0386:RSOTAP>2.0.CO;2

Wang, X. L., Swail, V. R., and Zwiers, F. W. (2006). Climatology and Changes of Extratropical Cyclone Activity: Comparison of ERA-40 with NCEP-NCAR Reanalysis for 1958-2001. Journal of Climate, 19(13), 3145–3166. https://doi.org/10.1175/JCLI3781.1

Westra, S., Alexander, L.V., and Zwiers, F. W. (2013). Global Increasing Trends in Annual Maximum Daily Precipitation. Journal of Climate, 26(11), 3904–3918. https://doi.org/10.1175/JCLI-D-12-00502.1

Yatagai, A., Kamiguchi, K., Arakawa, O., Hamada, A., Yasutomi, N., and Kitoh, A. (2012). APHRODITE: Constructing a Long-Term Daily Gridded Precipitation Dataset for Asia Based on a Dense Network of Rain Gauges. Bulletin of the American Meteorological Society, 93(9), 1401–1415. https://doi.org/10.1175/BAMS-D-11-00122.1

Yukimoto, S., Yoshimura, H., Hosaka, M., Sakami, T., Tsujino, H., Hirabara, M., … Kitoh, A. (2011). Meteorological Research Institute-Earth System Model Version 1 (MRI-ESM1) - Model Description. Technical Report of the Meteorological Research Institute, 64.

Zhao, T., and Yatagai, A. (2014). Evaluation of TRMM 3B42 product using a new gauge-based analysis of daily precipitation over China. International Journal of Climatology, 34(8), 2749–2762. https://doi.org/10.1002/joc.3872